University of Alberta

Nanofabrication Methods Towards a Photonically-Based Torque Magnetometer for Measurement of Individual Single-Crystalline Yttrium-Iron-Garnet Microstructures

by

Shawn R. Compton

A thesis submitted to the Faculty of Graduate Studies and Research
in partial fulfillment of the requirements for the degree of

Master of Science

Department of Physics

Spring 2012
Edmonton, Alberta

Abstract

This thesis describes preparation and nanofabrication of single crystalline yttrium-iron-garnet (YIG) for the purposes of ultra-clean torque magnetometry, as well as the design, fabrication, and testing of photonic crystal-based nanoelectromechanical systems for sensing applications.

A focused ion beam microscope is used to shape and manipulate epitaxially grown YIG, a section of which was milled into a disk capable of supporting a 3-D vortex-like state. This was placed onto a prefabricated silicon torsional resonator, which allowed a broad characterization of magnetic and mechanical properties.

Secondly, a photonic crystal-based sensor was designed in a silicon-on-insulator architecture and simulated with finite-difference time-domain methods. The final device properties were tested photonically and backed by further simulations. Once released, the mechanical properties of the system were characterized interferometrically, then photonically, showing the advantages to photonic based transduction schemes. The final device presents a platform for photonically studying magnetism, by use as a torque magnetometer.

Acknowledgments

This thesis you are reading as well as the research that went with it was a daunting task like I had not experienced before. Luckily I had many people to help me, guide me, and encourage me through my time at the University of Alberta.

I would first and foremost like to thank my supervisor Dr. Mark Freeman, whom provided the needed guidance and help to see this project to fruition. I am grateful for the opportunity he allowed me by taking on the role as my supervisor for the last two plus years. Without his wisdom I am not sure that this project could have been what it was in the end. Along with him, I would like to thank my many past and present group and journal club members Joe Losby, Jacob Burgess, Alastair Fraser, Steve Olson, Dr. Zhu Diao, Vince Sauer, Dr. Wayne Heibert, Fatemeh Fani Sani, Mung Kan, Rob McLeod, and Dave Fortin. Without your help and discussion many of the aspects of this project would not have been possible. The ability to bring ideas to a group of critical thinkers such as yourselves has lead to many wonderful suggestions with great potentials. I would also like to extend a special thanks to Dr. Doug Vick, who works absolute magic with the FIB.

Along with my many group and journal club members are my friends and co-M.Sc. students here at the University of Alberta Kyle Manchee, Marco Taucer, Sarah Regli, Mike Reid, Nick Arkell, and Laura Poole. You have put up with many nights of science jargon and assisted in making my time here in Edmonton as much fun as it has been. Although I was only in this city for a little over two years, I feel like we have managed to fully utilize it and ensure that we didn't waste any or our time here in Alberta.

My parents Polly and Ray and sister Tammy deserve a special place in this acknowledgment, as their constant support and motivation may be the only reason I have actually stuck with physics through the years. They have stayed steadily interested in my research and have always made sure I was enjoying myself, even though they were half of a country away. This also goes for all of my family and friends in Ontario, especially my Uncle Brian whom peaked my interest in science at an age when I could barely speak.

Finally I must thank my wonderful partner Amelia Walker. She not only agreed to moving to Edmonton in the first place but has ensured that all of my time for the last six years has been amazing with many adventures had and many still to come.

Contents

1 **Intro** **1**

1.1 Historical Time Line 1

1.2 NEMS Overview 3

1.2.1 Methods of Detection in NEMS 6

1.2.2 Applications of NEMS Sensors 9

1.2.3 Torque Magnetometry 11

1.2.4 Methods of Improving NEMS Detection and Responsivity 13

1.3 Photonics for NEMS 15

1.3.1 Fiber Optics and Optical Confinement 16

1.3.2 SOI Based Photonics 18

1.4 Convergence of Torque Magnetometry and SOI Based NOMS . 21

2 **Garnet** **22**

2.1 Introduction 22

2.1.1 Ferrimagnetic Garnets 22

2.1.2 Magnetic Vortices 26

2.2 Experimental 28

2.2.1 Material Choice and Composition 28

2.2.2 Sample Preparation for Bulk Magnetic Characterization 30

2.2.3 M-H Hysteresis 33

- 2.2.4 Sample Preparation for FIB Milling 35
- 2.2.5 FIB Milling of a Micromagnetic Disk 37
- 2.2.6 Silicon Paddle Mechanical Characterization 42
- 2.2.7 Silicon Paddle Torque Magnetometry 46

2.3 Conclusion 47

3 Photonics **50**

3.1 Intro 50
- 3.1.1 SOI Photonics for NEMS 50
- 3.1.2 FDTD Simulation Background 52
- 3.1.3 Photonic NEMS Detection Background 54

3.2 Experimental 56
- 3.2.1 Motivation for using NEMS in Photonics 56
- 3.2.2 Effective Index Study of Silicon 57
- 3.2.3 2-D FDTD Modeling of Photonic Elements 59
- 3.2.4 Photonic Crystal Design 61
- 3.2.5 3-D FDTD Modeling 65
- 3.2.6 Device Design and Fabrication 67
- 3.2.7 Photonic Testing of Fabricated Devices 70
- 3.2.8 Release of Photonic Paddles 74
- 3.2.9 Interferometric Measurement of Paddle 78
- 3.2.10 Photonic Mechanical Measurement of Paddle 80

3.3 Conclusion 84

4 Discussion **87**

4.1 Summary of the Fabrication of a Single Crystalline Magnetic Garnet Disk for Torque Magnetometry 87

4.2 Summary of the Design, Fabrication, and Creation of a Photonic Crystal Based Torsional Resonator 88
4.3 Progress Towards a Photonics-Based Torque Magnetometer . . . 88

List of Tables

2.1 COMSOL Frequency Downshifting Trends 45

3.1 Table of Device Design Parameters Used in the Final Chip Design 69

3.2 COMSOL Resonance Frequencies of Photonic Crystal Paddle, Simulated with Measured Parameters. 78

List of Figures

1.1 The Cavendish Experiment 2
1.2 MEMS Clamped Beam Resonance Example 5
1.3 Lock-in Amplifier Detection Schematic 6
1.4 Schematic of Interferometric Detection of NEMS 8
1.5 Torque Magnetometer Schematic 12
1.6 Diagram of Total Internal Reflection in a Fiber Optic Cable . . 17

2.1 Crystal Structure of YIG 23
2.2 Diagram of FIB Milling Mechanism 25
2.3 Simulation of Magnetic Vortex in a YIG Disk 27
2.4 Magnetic Hysteresis of LuIG Measured Using MOKE 30
2.5 FMR Spectrum of LuIG With the Corresponding FFT 31
2.6 SEM Image of YIG layers on GGG Substrate 32
2.7 Schematic For Measuring M-H Hysteresis Loops 34
2.8 Magnetic Hysteresis Of LuIG and YIG in High, Medium, and Low Magnetic Bias Fields 35
2.9 YIG Segment Mounted In FIB Chamber 37
2.10 SEM Image Sequence Showing the Milling of the Trench in YIG 39
2.11 SEM Image of Rectangular Membrane Attached to the FIB Micromanipulation Probe 40
2.12 SEM Image Showing A Comparison Between Milled YIG Disks . 42

2.13 SEM Image Sequence Showing the Sculpting and Placement of a YIG Disk onto a Silicon Paddle Torsional Resonator. 43
2.14 Frequency Response of YIG and Bare Silicon Paddle Resonators 44
2.15 FIB Platinum Repair of Torsion Rod 45
2.16 Magnetic Hysteresis Curve of YIG Measured Using a Silicon Paddle Torque Magnetometer. 47
2.17 Micromagnetic Simulation of YIG Disk With Fabricated Dimensions 48

3.1 Gaussian Mode Propagating in a Strip Waveguide Diagram . . . 51
3.2 Yee Cell Diagram Showing Field Calculation Points 53
3.3 Schematic Showing FSR Based Measurement Scheme 56
3.4 Effective Index Simulation of Silicon Strip Waveguides 58
3.5 2-D FDTD Simulation Power Profiles of Waveguide-to-Waveguide Coupling in Silicon 60
3.6 FDTD Simulation of a Single Line Defect in a Photonic Crystal 63
3.7 Transmission in a Photonic Crystal for Varying Filling Factors and Wavelengths, With Hole Radius Kept Constant 64
3.8 Transmission in a Photonic Crystal for Varying Hole Radius and Wavelengths, With Filling Factor Kept Constant 65
3.9 FDTD Simulation of 60° Bending in a Photonic Crystal 66
3.10 FDTD Simulation Model of a 3-D Photonic Crystal 67
3.11 Fabrication Dosage Curves Supplied by IMEC 70
3.12 SEM of Fabricated Photonic Elements Including Waveguide, Gratings and Photonic Crystals 71
3.13 Confocal Photonic Measurement Setup Schematic 72
3.14 Grating Coupler Output Spectrum 73
3.15 FSR Spectrums For Two Types of Ring Resonator Configurations 75

3.16 Etch Process Schematic For SOI Photonic Devices 76
3.17 SEM Top View of Released Paddle Resonator With Long Etch Slope 77
3.18 Interferometric Measurement Schematic For Photonic Paddles . 79
3.19 Interferometric Scan of the 1st Out Of Plane Mode in the Silicon Paddle Resonators 80
3.20 Plot Showing The Modes of the Piezo Buzzer Used For Actuation 81
3.21 FSR Spectrum of the Working Released Paddle Resonator . . . 82
3.22 Plots Showing the Photonically Measured Modes of the Working Paddle Resonator With Their Associated TM Noise Peaks . . . 83
3.23 Plot Showing FSR Peak Used With Over-layed Frequency Response Data From The Mechanical Oscillations 85

4.1 Photonic Crystal Paddle For Magnetic Sensing Proposal 89

Nomenclature

A	Cross-Sectional Area
AC	Alternating Current
BOE	Buried Oxide Etch
CMOS	Complimentary Metal-Oxide-Semiconductor
CPD	Critical Point Dryer
DC	Direct Current
E	Electric Field
EBL	Electron Beam Lithography
FDTD	Finite-Difference Time-Domain
FFT	Fast Fourier Transform
FIB	Focused Ion Beam
FMR	Ferromagnetic Resonance
FSR	Free Spectral Range
GGG	Gadolinium Gallium Garnet
GHz	Gigahertz

HeNe	Helium-Neon
IP	In-Plane
IPA	Isopropanol
kHz	Kilohertz
LLG	Landau-Lifshitz-Gilbert
LuIG	Lutetium Iron Garnet
MEMS	Micro Electromechanical Systems
MHz	Megahertz
MOKE	Magneto-Optic Kerr Effect
NEMS	Nano Electromechanical Systems
nm	Nanometer
NOMS	Nano Optomechanical Systems
OOP	Out-Of-Plane
PML	Perfectly Matching Layer
Q	Quality Factor
SEM	Scanning Electron Microscope
SOI	Silicon-on-Insulator
T	Period
TEM	Transmission Electron Microscope
TM	Thermo-Mechanical

Tm	Thulium
YAG	Yttrium Aluminum Garnet
YIG	Yttrium Iron Garnet
E	Young's Modulus
ε	Permitivity
f	Filling Factor
H	Magnetic Field
I	Moment of Inertia
l	Length
λ	Wavelength
M	Magnetization
μm	Micrometer
μ	Permeability
n	Refractive Index
ρ	Density
S_i	Silicon
S_iO_2	Silicon Dioxide
τ	Torque
t	Thickness
θ	Angle of Incidence

Chapter 1

Intro

This chapter will focus on torsional measurements and their progression throughout modern history. The scaling of devices from the macro to the nano in the form of NEMS is discussed. The methods to create, and advantages of such devices is covered, and the varying actuation and transduction schemes are described. Photonic-based devices are focused on in further detail, with background as to their mechanism for guiding light combined with some examples of recent uses.

1.1 Historical Time Line

The need to make measurements of minute forces has been present throughout history, ever since Newton's discovery of gravity. As the world of science became more complex, ingenious methods were conceived to measure such forces. A good example is the Cavendish experiment of 1798[1]. By utilizing a long wooden arm suspended from a very thin wire, small torquing forces acting on the rod lead to measurable deflections (figure 1.1). In this experiment the deflection of the beam was caused by gravitational forces acting between weights embedded in the beam, and outside weights whose position could be adjusted. With this technique Cavendish was able to measure very small force interactions (nanoNewtons), leading to a value for the density of earth to within a few percent of the modern day value. The Cavendish experiment was just one example of the incredible force sensitivities reached using mechanical deflections and force balancing, which adds emphasis to the fact that it was considered to be the state of the art technique throughout history.

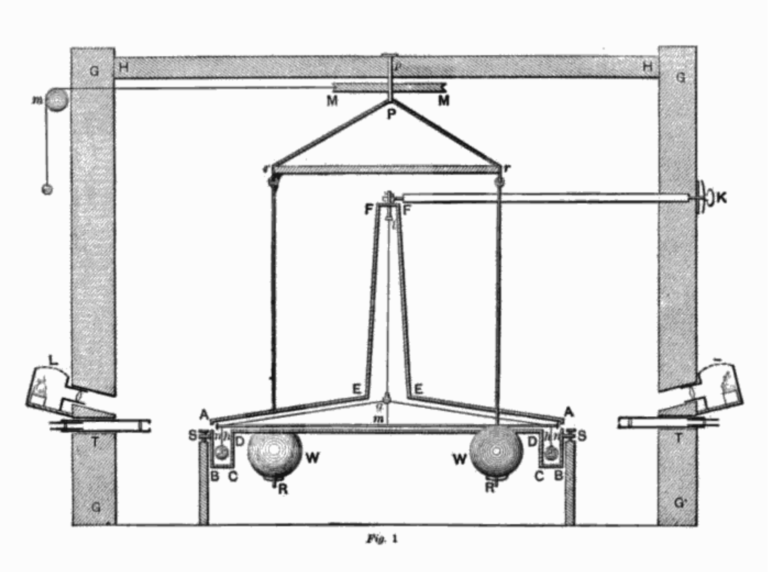

Figure 1.1: Diagram of the apparatus used to determine the density of earth by Henry Cavendish. The experiment was encased in wood to remove small fluctuations caused by heat and wind differentials across the system, and observed via glass telescopes (T) illuminated with lamps (L). Source: H. Cavendish. Experiments to Determine the Density of the Earth. *Philosophical Transactions of the Royal Society of London*, 88:469, (1798)

In modern times we have seen a resurgence of mechanical measurements following the pioneering of the field of micro-fabrication. The tools used to model and create new transistors on smaller and smaller scales, as well as the processing power generated by these new transistors, has lead to the ability to design and create objects on the micrometer and nanometer scale. By doing so, one is able to scale devices, such as a torsional oscillator, down to a scale where the resonant frequencies are extremely high, and losses are low. These two properties combine to form a new device capable of detecting forces on a sub attoNewton per root hertz scale[2]. As demonstrated by M. Roukes and A. Cleland in 1998[3], devices of this nature are able to replicate the experiments of the past[4] with incredible sensitivity to force, and relatively easy implementation. By shrinking a torsional oscillator to the micron or even sub-micron scales, electron charges on the order of $0.1e{\cdot}Hz^{-\frac{1}{2}}$ were able to be detected, and with optimization, predicted a possible achievable sensitivity of $10^{-6}e{\cdot}Hz^{-\frac{1}{2}}$. These measurements, and improvement on the original methods of fabrication[5] have sparked an entirely new field of research called nanoelectromechanical systems (NEMS). The basis for these fields is creating a small scale oscillator of some type with a set resonance frequency for specific modes, and utilizing the shift in resonance of the device caused by a small change in force. This small force can be applied by any number of methods including mass[6], magnetic force[7], capacitive force[8] and more[9], leading to the ability of these devices to be implemented in almost any sensing field.

1.2 NEMS Overview

When we scale resonator systems down to the micro and nano scales there are many advantages. Although the dynamics can in general be described using classical methods such as the Euler-Bernoulli beam equations[10] , one has to be cautious of the specific forces at play that govern the overall behavior of the system. To see the effects of miniaturization we can look at the clamped beam example. If we have a thin beam (thin meaning $t \ll l$) that is suspended across a gap but rigidly clamped at both ends, the motion can be described using the Euler-Bernoulli beam equation[11]:

$$\frac{\partial^4 u}{\partial x^4} = \frac{-\rho A}{EI}\frac{\partial^2 u}{\partial t^2} \tag{1.1}$$

Where E is the Young's Modulus, ρ is the density, A is the cross-sectional area of the beam and I is the moment of inertia, which in this thin beam case goes like $I \propto At^2$ with t in this case being the thickness of the beam. Solving this for the out of plane frequencies of oscillation yields.

$$f_n = \frac{C_n}{2\pi}\frac{1}{l^2}\sqrt{\frac{EI}{\rho A}} = C_n^{'}\frac{t}{l^2}\sqrt{\frac{E}{\rho}} \tag{1.2}$$

Where f_n is the n^{th} out of plane mode, C_n is the n^{th} numerical constant, and l is the length of the beam. From this equation it becomes clear that as the length of the beam is reduced the frequency increases, which means the majority of MEMS devices work in the kHz to MHz range, leading to very high sensitivity and low frequency noise[12]. A simple simulation depicting the first four out of plane modes of a beam suspended across a gap can be seen in figure 1.2. Each successive mode shows one more nodal point than the solution to the eigenfrequency before it, and each mode getting progressively higher in frequency.

Another fairly obvious side effect is the reduction of mass of the system. As we scale the devices down in size, the mass ratio of anything you would like to measure to the mass of the resonator itself becomes larger. This means that the overall effect of mass loading on the system is greater, leading to a more easily detectable signal change. This property has lead to many attempts to use MEMS and NEMS devices as mass sensors and mass spectrometers[13, 6].

As with most things, there is a limit to the benefits of a reduction in size. In the above case, even though the mass of the system is reduced, the target area of the device is also reduced, making it harder to physically land particles

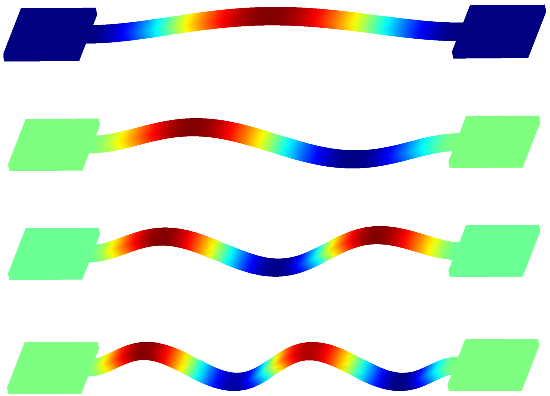

Figure 1.2: Image showing the first four out of plane modes of a clamped beam resonator, as simulated in COMSOL finite element modeling software. As can be seen the higher order modes have more nodes and also higher frequencies, which in order are: $f_1 = 210kHz$ $f_2 = 580kHz$ $f_3 = 1.12MHz$ $f_1 = 1.86MHz$

for detection. Also with shorter devices, the spring constant becomes larger, leading to higher stiffness and less responsivity to impinging forces. This can be explained once again using the doubly clamped beam example from above. If we treat our beam as a simple mass and spring apparatus then it becomes straightforward to determine an effective spring constant for a loading force at the beams center, which is as follows[8]:

$$\kappa_{eff} = 32E\frac{t^2 w}{l^3} \tag{1.3}$$

From this it becomes clear that with a reduction in l, the force constant cubically increases. This can be alleviated by a similar reduction in thickness and width of the devices, but this causes such a serious downsizing that the devices become hard to detect and have similar sensing area problems. This is not to say that it is not advantageous to decrease the sizes of devices if capable, but optimization must occur on a device by device basis and cannot be generalized to the entire field of NEMS.

By understanding these scaling effects, one can take advantage of these small devices for practical purposes. With such high sensitivities and low cost of production due to the semiconductor industries expertise in silicon, the only issue is how to detect the very high frequencies and very small deflections associated with the most sensitive of the devices.

1.2.1 Methods of Detection in NEMS

One of the main complications present with NEMS is the detection scheme. With devices reaching very high resonance frequencies (upwards of 1GHz[14]) and becoming increasingly small[15], detection of the resonance becomes non-trivial. Whether one wants to measure a DC downshifting in a resonance peak due to mass loading[6], or an AC modulation of the resonance peak location in frequency space caused by a varying force across the device[16], the detection is similar.

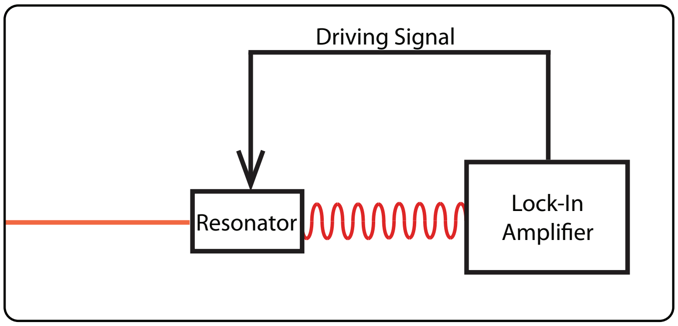

Figure 1.3: Schematic showing the detection scheme for lock-in amplification based NEMS sensing. The lock-in amplifier supplies the driving signal as well as measuring the response.

First the resonance of the device must be actuated using some varying external force. This can be anything from mounting the system on a piezo transducer to using photon pressure from a tapered fiber coupled to your system[17]. The signal being read out is then modulated by this actuation to some extent, and that modulation it picked up with a lock-in detection.

By generating the reference, and measuring the signal from the device, the lock-in amplifier is able to determine the amplitude of the signal modulation at that specific frequency. The general setup of this type of system can be seen in figure 1.3, and has many advantages including the reduction of white noise due to small frequency bandwidths for measurement. In this setup when the device is on resonance, the amount of signal increases dramatically due to amplification in signal at that resonance proportional to the device Q factor. By sweeping the frequency of the lock-in amplifier, the resonance of the device can be traced, resulting in a spectrum showing it's center frequency and width. With this information the shift in the frequency of the resonator caused by the application of an external force can be measured, with as much precision as the measurement system and the width of the peak allows.

To actually measure the signal from a device a multitude of techniques have been developed, each having their own merits. Some of the more common methods include Fabry-Perot interferometry[18], capacitive coupling[19], piezo-resistivity[20] and more recently photonic[21]. The choice of method comes down to the type of force you would like to measure, and the equipment at hand.

The Fabry-Perot interferometer works by having two paths for the light to travel, where one path stays constant as a reference and the other is allowed to vary in length. This setup can be seen in figure 1.4, which shows the path of the light and the corresponding modulation pattern. The impinging light reflects off of the back of the cavity and constructively or destructively interferes with light reflecting off of the NEMS device. As the NEMS device resonates the path length change causes a modulation in the signal at the resonance frequency. This signal is sent to a photo diode and can be picked up by a lock-in amplifier. Interferometric measurements using a Fabry-Perot

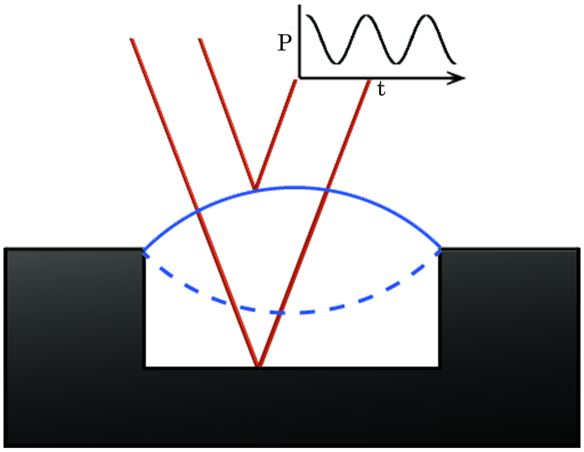

Figure 1.4: Diagram showing the method for interferometrically measuring the resonance of a NEMS device. As the beam reflecting off of the device and the beam reflecting off of the underlying substrate interact, a modulation in power is seen due to constructive and destructive interference.

cavity are easy to implement in silicon-on-insulator (SOI) architectures, since the etching of the oxide layer gives a smooth and highly reflective back surface for the interferometer. The only requirement for this is a semi-transparency to the incoming laser, which helium-neon (HeNe) lasers fit for silicon, making them ideal due to their cost effectiveness. This method is one of two main methods used throughout this thesis, as it is relatively easy to accomplish with high sensitivity.

The other methods mentioned above involve special preparation for implementation. In the capacitive case the detection is based off of the modulation of the distance between two metallic surfaces acting as a parallel plate capacitor. This means that it requires a metallic coating on both the device and a nearby area. By depositing metal on the MEMS and a nearby surface, the capacitance can be used both to actuate resonance via capacitive force, as well as measure resonance via the voltage modulation generated when the gap between the parallel plates is changed. This method clearly requires added care and post-processing of the devices, leading to more complex systems. For this reason it was not ideal in measuring the devices presented. The piezo-resistive case involves a careful deposition of a piezo-electric material along the device, and two conductive pads. As the material is stressed from oscillations, the resistance changes and can be read out through the conductive pads. The deposition of material in this case must be precise, and of a material that expresses high piezo resistivity. Because of this, this method falls into the same category as capacitive measurements for being non-ideal for this project.

1.2.2 Applications of NEMS Sensors

With so much variation in how devices can be measured, NEMS and MEMS are capable of acting as sensors for an wide array of applications. As mentioned in a previous section, devices of this nature have been implemented in detection schemes for many uses, including mass sensing, electrometers, and magnetometry. With research constantly improving the fabrication and detection of devices, the number of uses is constantly increasing, leading to a higher applicability to industry.

When a force acts on a resonating device is some way, the resonance will shift. This happens because the dynamics of resonators are very sensitive to any change, which means that as long as you are able to turn what you would like to sense into a force, which can act upon the resonator, you can measure that change. This is a general way of saying that NEMS are capable of acting as a sensor for many uses in today's modern world. To help understand this one can look at the simple example of adding mass to a resonating beam. When mass is added to the system the total mass changes, and with devices approaching the nanoscale, these changes can cause a measurable signal. This addition of mass manifests itself as a downshift in the resonance signal as per equation 1.2, which can easily be measured with high quality factor (Q) devices and lock-in detection schemes. Correlating the shift in resonance to an increase in mass, results in a measurement of the amount of material that has bound to the resonator. Due to the fact that the mass of the resonators can be very low and the Q can be very high, the masses on the order of a zeptogram can be measured to high precision[22]. Furthermore with some well thought out designs and the appropriate equipment, one can even measure this mass change in real time leading to signals corresponding to stepping down in resonance by steps of these single molecules[6, 13]. This type of sensor can be used to measure the mass of molecules or simply to tell you if specific molecules are present in the system. The latter of these arises from tailoring your resonator to a specific binding agent by functionalizing the surface. By having an array of resonators, each looking for a different biological tag, NEMS can be used as medical sensors for certain diseases. Devices of this nature are currently being made at the Indian Institute of Technology with hopes to be in use in India as an inexpensive method of mass screening for heart disease[23]. A similar method can also be used to detect explosive molecules in their vapor form. This is done by coating a cantilever in an explosive specific binding agent and calibrating for the signals produced by each type of molecule[24].

As mentioned previously, NEMS can also be applied to magnetic sensing. This is done by depositing magnetic material onto a resonator and measuring the response to the interaction with an applied magnetic field. When a magnetic field is applied, the spin torque felt by magnetic moments in the material transfers into a mechanical torque, causing a force to act on the cantilever. This force shifts the resonance, and can be detected by a lock-in scheme described in figure 1.3. By applying a large field to align all of the spins in a material, and simultaneously applying a second magnetic field, which is time-varying, the precession of the spins as they return to their previous state can be studied. Other properties of the magnetic material are also available to be measured through careful fabrication and detection of the devices, including vortex creation and annihilation in disks[25], and domain wall shifts in bar magnets[26]. To achieve the sensitivities needed for these measurements, the methods used by Cavendish and Coulomb are revisited, and torsional NEMS devices created.

1.2.3 Torque Magnetometry

Using torsional resonators as magnetometers is a time tested technique[27]. This is due to their abilities to measure magnetic properties with extremely high sensitivities in the presence of very large magnetic fields. With the improvements in micro and nanofabrication techniques, devices of this type can be scaled down to the MEMS and even NEMS scales, giving them all the benefits described in the previous sections. With a plethora of commercial applications that utilize magnetic fields, many of which on the micro and even nano scales, this scaling becomes an ideal way to measure properties of individual magnetic elements separate from the bulk.

The main concept of a torque magnetometer is that a magnetic material is placed on a torsional resonator and a large bias field is applied. A diagram of such a system can be seen in figure 1.5 showing the general orientation of vectors. Due to magnetic torque $\overrightarrow{\tau} = \overrightarrow{M} \times \overrightarrow{H}$ the resonator can be effected in two ways. The first being that the resonators spring constant can stiffen, leading to a shift in the resonance signal and the second being that magnetic dissipation can be produced acting on the resonator to effect the Q. By measuring these changes one can infer many properties of the magnetics of the system including its general energy landscape.

On the micro- and nano-scales, the concept is the same, except the reso-

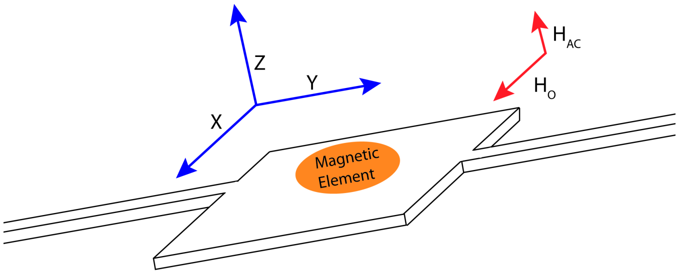

Figure 1.5: Schematic showing the field orientation in a NEMS torque magnetometer. The large in plane field H_O is applied to align the magnetization to a specific direction, which in this case would be the x direction, while the time varying H_{AC} leads to an out of plane torque.

nance frequencies can be on the order of ~100MHz, and the quality factor can be on the order of $\sim 10^5$. This means that the effects from very small elements can easily be measured, as well as any small changes to these magnetic systems. This technique is so sensitive that it has already been used in several applications including measuring thin magnetic film deposition with a resolution of 0.3nm[28], as well as domain wall propagation in a bar of magnetic material [26]. With low power consumption, relatively easy integration, operations in high fields, and the ability to be cooled, which adds many benefits to the mechanical properties of the devices, the field of torque magnetometry has enormous potential in future applications.

Looking at figure 1.5 we can see the setup for measuring the magnetization switching in a sample of magnetic material due to an external bias field. A large in plane bias field causes the spins to align in one direction. When a pulsed secondary field is applied out of plane the spins are disoriented, and due to conservation of angular momentum they precess until returning to their original position. This precession causes a magnetic torque on the spins, which couples to the mechanical torsion of the system leading to a shift in resonance. By tailoring the shape of the magnetic material on the magnetometer, one can cause features in the magnetization arising from shape anisotropy, such as domain wall shifting and vortex creation/annihilation. These states can be used to probe the local energy landscape of the material by looking at their interaction while translating them in the system. A common artifact when looking at such fine resolution is the presence of local pinning of the state based on magnetic inhomogeneity in a crystal, which for example can arise from grain to grain variation in the crystalline anisotropy axis. This type of feature appears as step-like noise in a simple magnetization vs. bias field hysteresis loop[29].

A setup of this nature was used in the 2nd chapter of this thesis and was the inspiration for creating a photonic crystal torsional paddle. The torsional mode of a clamped beam resonator is an obvious choice for use in torque magnetometry, as the design and implementation can be straight forward due to SOI technologies. If the orientation is chosen accordingly the torques on a magnetic material can actuate the torsional eigenmodes of a device. With theory implying that the mechanical and magnetic resonances in a system can couple together to give magnetically actuated mechanical switching[30], studying and improving on both resonators and magnetic materials could lead to low-power switching applications for storage technologies.

1.2.4 Methods of Improving NEMS Detection and Responsivity

With such a high versatility in measurement and detection NEMS are an exciting avenue for research exploration in both the university and industrial settings. The number one goal of most current research is probing smaller and smaller effects, which means increasing the sensitivity of devices. As discussed in a previous section, one way to accomplish this is by scaling the system down. Although this provides a high increase in sensitivity of devices, there are many adverse effects, such as a shrinking of the target area on a resonator. To further increase the potential for NEMS is it important that the materials and techniques be taken into considerations, especially their limitations in measurement schemes. For example the cooling of a resonator effectively removes thermal fluctuations in the system and can lead to devices with Q's several times larger than at room temperature. This can yield much more sensitive measurements, but is non-ideal for several reasons, the most important of which is the commercialization aspect. In schemes like this detection can also become an issue, as any windows to allow interferometry to be preformed also allow heat to enter the system.

Along a similar line with cooling, is placing devices in vacuum to reduce friction and mechanical dissipation. This can have a very dramatic effect on the properties of the system, allowing one to see things such as thermomechanical noise[31]. With a simple vacuum system one is able to increase the quality factor of resonators by upwards of a hundred times, as well as heavily reducing the noise in the measurement. Although this is common place for many MEMS and NEMS measurements to date, this is still a non-ideal avenue for commercialization due to the high costs associated with containing sensors in vacuum.

A different avenue of pursuit is other detection mechanisms and schemes. With the invention of integrated photonics some groups have been able to detect devices by using the silicon layer of SOI as a waveguide, and measuring the modulation of the light due to mechanical movement[32]. This has many advantages over other detection schemes, as it does not require additional layers of material for detection, and greatly reduces thermal effects if the measurement wavelength is chosen outside of the absorption band. By confining the light inside waveguides, defined using regular CMOS processing, the creation of NEMS sensors is moving in the direction of integrated lab on a chip technology. Since the processing is similar to that of the microelectronics industry, these systems will eventually be capable of integration with modern electrical systems. Utilizing total internal reflection in a similar manner to that of fiber optics, nano-optomechanical systems (NOMS) have the potential to improve existing NEMS devices in a commercializable way and can be further improved upon by both vacuum and cooling.

1.3 Photonics for NEMS

Due to its very low losses and high speed, the modern day telecommunications industry is making a switch to using light as its source wave for information transfer. With the invention of practical and commercializable fiber optic cables, along with the realization of the data transfer rates achievable by such cables, light was a natural progression from electrical systems. Although light provides a good alternative to electricity, most of the modern technology is still is, and most likely always will be, based on silicon microelectronics, thus regular fiber optic size scales are ultimately too large for any form of integration. This is where SOI photonics can play a large role since the methods of fabrication, and device architectures follow that of the electronic industry.

Technologies using the confinement of light are not only advantageous from a industrial point of view, but also provide highly sensitive systems for research. By using photonics one is able to confine light of wavelength on the order of microns to waveguides less than 500nm in size, and by utilizing changes in the refractive index of such waveguides can sense very small changes to the devices. This new field is still mostly up-and-coming, but has enormous potential for future developments and is the focus of Chapter 3 of this thesis.

1.3.1 Fiber Optics and Optical Confinement

Following a historical parallel with the development of modern electronics, integrated photonics is still very much an emerging field. Although there are a wide array of industrial uses many technologies are being developed, especially in the area of sensors[33]. As fiber optics became well understood, and manufacturing was able to produce cables of needed quality, the infrastructure for data transfer made the switch to light. With a modern fiber optic cables having a much higher data transfer rate than their electrical counterparts, and significantly less attenuation of the signal, it is easy to understand why the focus was switched to optical telecommunications. As with most technologies, once industry adopted it, cost was lowered and quality was raised allowing integration into research labs worldwide.

To understand the potential of fiber optics it is best to look at an example of how the propagation of light in a fiber works. The main concept is based off of total internal reflection which can be simply understood using Snell's law.

$$n_i sin\theta_i = n_t sin\theta_t \tag{1.4}$$

Where n_i is the index of refraction in the incident material, θ_i is the angle of incidence of the incoming light, and n_t and θ_t are the same for the transmitted light. This tells you that light will be bent in different materials based on the index of refraction which is a ratio of the speed of light in vacuum to the speed of light in the material. Since the transmitted angle is based off of both the index in the incident material and the index in the transmitted material we can now look at when the light will be reflected based off of the chosen materials. This is equivalent to asking when the transmitted light's angle will be ninety degrees. Rearranging the equation and solving for $\theta_t = 90°$ gives us:

$$\theta_c = arcsin(\frac{n_t}{n_i}) \tag{1.5}$$

where θ_c is the critical angle for total internal reflection. By making the right choice of materials, and surrounding a higher index material (core) with a lower index material (cladding) one can cause the light to always be reflected when propagating down, hence the name total internal reflection. As can be seen in figure 1.6 as long as the light is at an angle larger than θ_c , it will continuously reflect off of the core-cladding boundary. With typical index values in modern optical cables being 1.52 for the cladding and 1.62 for the core[34], as long as the light is aligned to the input with a specific angle, propagation down the fiber will occur with very little losses at the speed of light in the material. If the core size is too large, multiple transverse modes will be supported in the cable. These modes have multiple nodes along the transverse direction in the core. This type of fiber is called a multimode fiber, and has much higher losses than its single mode counterpart due to mode dispersion[35].

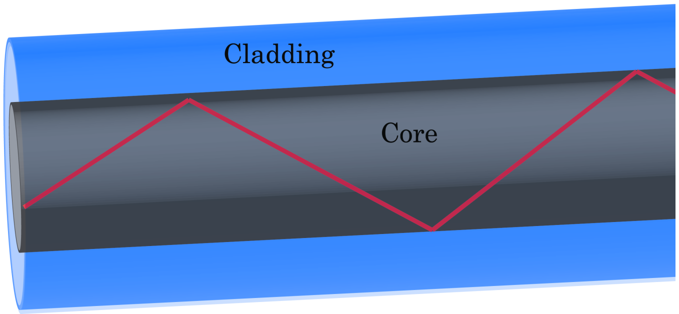

Figure 1.6: Diagram showing the propagation of light in a fiber. Once the light has managed to enter the fiber within a certain acceptance angle, the beam can propagate indefinitely due to total internal reflection.

If we take the fiber optic cable system and shrink it into the micro scale using microfabrication techniques, we get the field of integrated photonics. Although the size scale is much smaller, the principles at work are similar to those in the fiber optic case but with a few additional effects. By using silicon as the propagation material and silicon dioxide and air as the cladding materials one can create waveguides on the order of 500 nm width to confine and direct light with bend radii on the order of microns. This field has allowed the creation of very small scale sensors using the benefits of light as a source wave, and has lead to a high interest in the research community for pushing the limits of fabrication and sensitivity of such devices[33].

1.3.2 SOI Based Photonics

Very pure crystalline silicon on insulator material such as silicon dioxide can be easily obtained thanks to its use in modern electronics. These wafers have a thin layer of silicon (220 nm in our case[1]) on top of a thicker layer of insulator (S_iO_2). By using patterning techniques developed by the electronics industry one can define all kinds of very fine structure in the silicon layer of the wafer, etching away unnecessary material. This type of system was first demonstrated in 1988[36], with strip like waveguides appearing in 2006[37]. As stated above these systems provide an ideal architecture for integrated photonics since n_{S_i}≈3.5 and $n_{S_iO_2}$≈1.5 with air or vacuum being very close to n∼1[38]. Although the main challenge is to direct light into a waveguide via in-plane scattering, once the light is in the system it can be easily directed via total internal reflection[2].

The key difference in shrinking the system is the evanescent tail of the propagating wave that exists outside of the waveguide. By utilizing the fact that this tail can be used to transfer light into a supporting mode in a second waveguide in close proximity the original, many interesting devices can be

---

[1] A quick calculation of the propagating wavelength in silicon for 1550 nm light gives: $\lambda = \lambda_O/n_{S_i} \simeq 440\,nm$, meaning a thickness of 220 nm is $\sim \frac{\lambda}{2}$.

[2] With an operating wavelength of 1550 nm being below the bandgap in S_i, propagation can occur with very low optical absorption.

made. What this means is that light can be transferred between different systems on the same chip, allowing integrated devices to be made[39]. All of this is achieved using a single SOI chip, with minimal post-fabrication alignment needed due to the on-chip architecture.

As stated above one of the main problems in silicon photonics is the initial injection of light into the system. In our case this is done using a scattering source that takes angled out of plane light and scatters it into an adiabatic taper feeding into a waveguide. This device, known as a grating coupler, is a two layer system consisting of rectangular ridges. These ridges act as scattering sites, causing the light to propagate in plane. This works on the principle of interference, which results in the couplers having a strong dependence on frequency, leading to an acceptance band of tens of nm in wavelength. The light that is scattered in plane is injected into the waveguide via a tapered section, which tailors the mode shape to that of the waveguide by compressing the light. With a single mode propagating down the waveguide, this light can then be guided into further devices.

One main category of device that can be fabricated is known as a photonic crystal[40, 41]. This is made here by creating an array of periodic holes in the silicon layer, which act as the lattice points in a crystal. When defects are introduced in the form of hole size variation or removal, the light can be guided. This stems from the fact that similar to a normal crystal, photonic crystals have a band structure, and hence are able to contain the light at the boundaries of the defect. This form of device is a main focus of this thesis and will be discussed in chapter 3.

With the ability to fabricate and utilize photonic systems becoming more accessible, combined with the inherent sensitivity to changes near the light path due to the evanescent tail, using photonic devices as sensors was a natural progression. When there are small material changes near the waveguide light path, the light will travel at a different rate through that material. This is due to changes in the refractive index from a change in material properties, and since the mode also exists outside of the waveguide through it's evanescent tail, it is effected by these close proximity index changes. The new mode shape can be defined using the effective index formalism, which gives the average index as seen by the light. By causing modulations in this effective index, modulations in the traveling mode can be seen. This form of sensing has been extended into the mechanical sensing regime by utilizing NEMS devices[42].

In 2008 Tang *et* al. began using the benefits of on chip photonic sensing to improve sensing and actuation in NEMS devices[42]. By releasing a section of a waveguide with a carefully tuned etch gap they were able to actuate the motion of the beam by utilizing photonic pressure, similar to optical tweezers. They were also able to measure the modulation in the signal using a simple lock-in method. The benefits of using this methodology became apparent, including very high sensitivities, high detection bandwidths, and low losses. Further improvements were made in 2010[21] when, as suggested in the 2008 paper, the mechanical section was released inside of a high finesse optical ring resonator. By circulating the light many times in very high Q optical cavities, constructive interference allows a build-up of optical energy density. With much higher energy density, the sensing region become more sensitive to subtle changes, leading to a superior device. Further improvements to elements of the NOMS carried out by the Painter group by utilizing photonic crystal structures to guide and confine light, have shown that even higher frequency devices are capable of being fabricated and measured[17]. With all this in mind it is clear that photonic based detection of NEMS systems is the next generation of NEMS sensor technology. With such high industrial applicability and integration into already existing complimentary metal-oxide-semiconductor (CMOS) systems the technology is capable of creating lab on a chip sensors for many applications.

1.4 Convergence of Torque Magnetometry and SOI Based NOMS

By combining these two technologies, one can envision a photonic based torque magnetometer. This is the ultimate goal of this project, as increasing the sensitivity of a magnetometer improves the measurement of all subsequent magnetic properties. By creating a SOI based photonic device, shaped in a similar manner to regular torsional magnetometers, and releasing these devices post fabrication using wet etching, a SOI based photonically measured torque magnetometer can be made. By also utilizing high optical Q cavities to increase the optical density in the sensing region, the hope is that sensitivities can be reached, which are higher than those currently achievable in regular detection methods. One stipulation of this method is that it requires exact placement of magnetic material, as coating a section of a waveguide can severely alter the effective index in that region. This means that one can consider using a focused ion beam microscope for manipulations onto an already released resonator, which opens the door to the possibility of measuring epitaxially grown, single crystalline material.

Chapter 2

Garnet

This chapter will cover the making and characterization of a Yttrium Iron Garnet (YIG) disk placed on a torsional resonator. Mechanical and magnetic characterization of this system was carried out experimentally, as well as theoretically using detailed simulations. The results of this project are outlined in full, with an indication of possible applications that a device of this nature might allow.

2.1 Introduction

2.1.1 Ferrimagnetic Garnets

Rare earth garnets have been studied extensively since their discovery in 1950[43, 44]. These materials have a very ordered structure, which can be seen in figure 2.1, and well defined magnetic properties[45], making them ideal for testing magnetic detection systems. Being fairly rigid, with a low ferromagnetic resonance (FMR), the garnets (YIG especially) become an ideal choice as a candidate for magneto-mechanical coupling[30]. Rare earth garnets are also known to have some of the highest Verdet constants[46], allowing them to be integrated into magneto-optic systems due to the high associated Faraday rotations. YIG especially ($Y_3Fe_2(FeO_4)_3$) provides an excellent platform for microwave applications because of its high Q in the microwave frequency range[47]. By isolating a small element from an epitaxially grown thin film, single crystallinity can be assured, resulting in a clean and well defined magnetic element. This can be accomplished using a variety of methods [48, 49], but it has been found that for the control needed the focused ion beam microscope (FIB) provides an ideal method of fabrication, with the only caveat being possible ion damage[1].

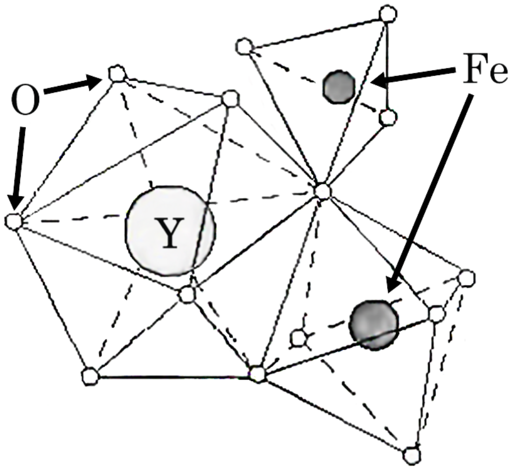

Figure 2.1: Diagram showing the crystal structure of YIG ($Y_3Fe_2(FeO_4)_3$). As can be seen the two iron sites are non-equivalent, which is what leads to the ferrimagnetic nature of the material. Both the yttrium and the iron are contained in ordered structure made of oxygen. This image has been adapted from http://www.larsenglish.com/magneticresonance

To shape and manipulate YIG, a FIB was used. The general principle of a FIB is similar to that of an scanning electron microscope (SEM). By sending current to a sharpened tungsten tip, that has been wet with a layer of liquid gallium, gallium ions are emitted in a well defined Gaussian beam. This is due to the high fields present at a focused tip, effectively causing a field emission

---

[1] Studies made by Alastair Fraser have demonstrated negligible damage if care is taken[50]

of ionized gallium. Although the tip is exceedingly sharp, on the order of a few nanometers, there is a finite limit to the shape of the wetted gallium layer ($\sim$ 5nm)[51] due to emission of gallium ions at high fields, which can reach upwards of 10v/nm. The resulting shape is known as a Taylor cone[52], which leads to a steady emission of gallium ions from the tip as the liquid source constantly replenishes emitted atoms.

The FIB has been shown to be a versatile tool, especially within the semiconductor industry. By utilizing its ability to "cut" away material and view cross-sections, analysis can be conducted on transistors, which cannot easily be done using any other method [51]. Some of the other known uses of the FIB include preparations of transmission electron microscope (TEM) grid sample[53], repairing defects in photolithographic masks[54], and rapid prototyping of variations in NEMS. The latter of these is of the most interest to this thesis and will be the focus of the coming chapter.

When the FIB is in milling mode, ionized gallium atoms are emitted at the sample surface, which interact with the sample sputtering away material as seen in figure 2.2(a). This provides a method to mill well defined shapes into almost any material, which in turn leads to a rapid prototyping of NEMS designs. By using a variety of beam currents, and differing shapes, NEMS can be created as cantilevers, clamped beam, and even torsional bars. Additionally with field emission ion microscopy, as well as an integrated SEM, work that is being done can constantly be monitored to assure that progress is being made.

The beam profile of the gallium ions forms a Gaussian shape. This shape needs to be taken into account when milling structures, as the tail end of the Gaussian can remove extra material. To ensure that the designed shape is constructed efficiently small milling currents can be used, and software recipes can be chosen based on the material type. This allows control over how flat a

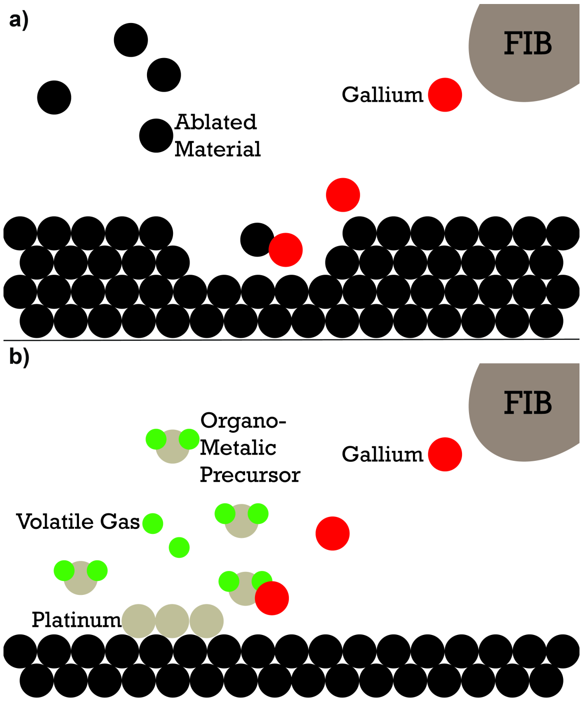

Figure 2.2: Diagram showing the process of (a) FIB milling using gallium ions, and (b) deposition of material onto a surface. The energetic ions are emitted from the tip, allowing them to either ablate material, or breakdown an organo-metallic gas.

surface can be made, as well as how sharp of features can be milled. As with most techniques, there is a finite limit to this due to a minimum operational beam current, time constraints, and redeposition of sputtered material.

Sputtered material has a tendency to redeposit in the vicinity of features being cut. This means that careful measures must be taken to assure that material deposition does not occur. The usual approach to this is milling channels, also known as blow-out holes, for the material to travel through. By milling such structures, elements can be designed with a greatly improved success rate to offset the time consuming FIB process. With little-to-no redeposition in the device area, structures can be milled without concern of destroying mechanical properties or even the devices themselves.

As alluded to previously, FIB techniques can be used to not only mill but also deposit material for repairs. This is done by injecting a gas into the chamber prior to milling. By using specialized gasses that react with the secondary electrons produces by the gallium ions, material can be deposited along the beam path, creating a method to quickly repair structures figure 2.2(b). This works by having a gas containing components that will become volatile and components that you would like to deposit. When electrons or gallium ions interact with this gas, the volatile components evaporate and leave behind the intended material to be deposited. Since the material depends only on the source, many sources are commercially available to use for deposition including some metals as well as magnetic materials[55, 56, 57]. The ability to repair damage to the system increases the robustness of this technique, further demonstrating it as an ideal choice for rapid prototyping of NEMS.

2.1.2 Magnetic Vortices

Micromagnetics is a field of very high interest due to its numerous industrial applications[58, 59]. To help better understand what is occurring in ferromagnetic systems, they can be fabricated on the nano scale, which allow cleaner probing of the magnetic properties. If the shape of this element is then confined to a disk, a magnetic flux closure can occur, resulting in a magnetic vortex[60]. This happens when a large shape anisotropy in the material causes the spins along the edges to curl. This progresses throughout the sample until the geometrical constraints are too high, forcing the magnetization out of the plane of the disk. This out of plane magnetization is referred to as the vortex core, with the curling magnetic field known as the vorticity and can be seen in figure 2.3. The core of this vortex is constrained in size, meaning it is affected by things on very small size scales in the local vicinity. By applying a large bias field in the plane of the material, the vortex core can be pushed to the edge, which causes it to annihilate as it leaves the sample.

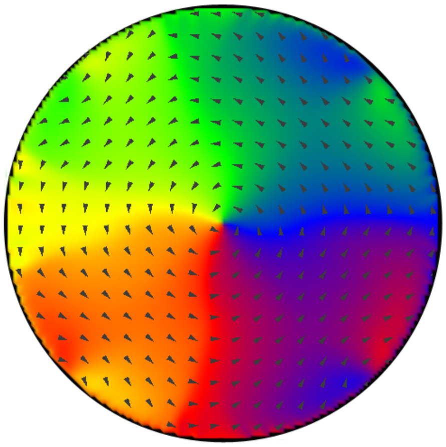

Figure 2.3: Simulation of a magnetic vortex showing the alignment of spins due to geometrical constraints. The color map and arrows show the direction of the magnetization in the sample, with the simulated disk having a diameter of $\sim 1.2\,\mu$m. This simulation was done using LLG Micro-Magnetics by Jacob Burgess.

Vortex formation in a magnetic system is mediated by several properties, including shape and magnetic properties of the material. By using the in-plane bias field to force the vortex core off of the center of a disk, the core can be used to probe the local energy landscape of the material. If it encounters any defects in its path, pinning can occur from a local energy minimum, which can lead to abrupt movement of the vortex core. By placing such a device onto a nano-torsional system, the movement can be measured by local torques being applied via a second out of plane dither field. This gives an ideal method to measure hysteresis of an individual disk as opposed to other methods such as magneto-optic Kerr effect (MOKE), which requires an array of disks to obtain an appropriate signal[61].

By utilizing a FIB to mill magnetic rare earth garnet material (YIG) into micro-disks, and placing these disks onto torsional resonators, magnetic characterization of the YIG can be achieved with very high sensitivity and control.

2.2 Experimental

2.2.1 Material Choice and Composition

Although there are many magnetic materials that can be deposited using simple processes, none of them have properties quite similar to those of YIG. With one of the motivations for studying magnetic NEMS being the possibility of magneto-mechanical coupling[30], which is the control of sample magnetization through mechanical motion, YIG becomes a good choice of material. This is because the FMR signals obtained from YIG samples are small in comparison to other materials (∼200-500 MHz). Due to the fact that for maximum coupling, the magnetic resonance signals need to overlap with the mechanical resonance of the system, the lower the frequency the easier the fabrication and detection of the NEMS becomes. Additionally epitaxially grown YIG is single crystalline, which allows a “cleaner” measurement of magnetic features such as vortices and domain walls. With less crystal inhomogeneity to act as local pinning sites, the magnetic feature is free to propagate through the material. A combination of such properties made the study of YIG essential to this project, but added complications such as how to manipulate nano or micro sized elements of a thin film onto a NEMS device.

Magnetic garnets are a historically widely studied field of materials[45]. This is because they have very well understood magnetic properties, making them ideal for calibration in many cases, such as magnetic hard drive read head characterization. As stated previously, these materials were chosen for study in this experiment due to many of these very properties, and wafers of epitaxially grown Lutetium Iron Garnet (LuIG) and Yttrium Iron Garnet were obtained (Ilyashenko Group Moscow State University and Shin-Etsu Chemical Co. ltd respectively). Extensive characterization of the LuIG was carried out by a previous colleague of mine, Alastair Fraser, who laid the foundation for a component of this project. When analyzing the hysteresis of the magnetization in bulk LuIG as shown in figure 2.4, it is easy to see that there is some kind of anisotropy in the signal. The two shapes indicate at least one easy-axis present, meaning a location with preferable alignment of the magnetization in the sample. This axis is caused by the crystal structure of the material and must be taken into account when making devices to study various magnetic effects. Further complications arise when looking at the FMR signal of LuIG. A sample ferromagnetic resonance (FMR) signal obtained by Alastair Fraser can be seen in figure 2.5(inset) with the main figure showing a Fast Fourier Transform (FFT) of the signal to determine the frequencies present. The figure shows the complicated behavior of the LuIG and furthermore, calculations using the well known Kittel relationship[62] do not match the trend of the data[50]. With this in mind, the samples were taken to the University of Alberta Electron Microprobe Laboratory for material compositional analysis.

The analysis at the microprobe facility was done using a CAMECA SX100 electron probe micro analyzer, with Yttrium Aluminum Garnet (YAG) as a calibration stub. By using a material of known composition and looking at the energy-dispersive X-ray spectrum, computer analysis is able to determine the composition by percentage of the material in question. Analysis was carried out on both the YIG and LuIG samples and showed that although the composition of the YIG sample is pure as stated from the supplier the LuIG actually contain almost no lutetium. The LuIG[2] was shown to consist of mostly thulium (Tm) and gallium with very little lutetium in the composition. This could explain some of the discrepancies from the Kittel equation, and caused YIG to be used

---

[2] Although determined not to contain lutetium, the sample material will still be referred to as LuIG for simplicities sake

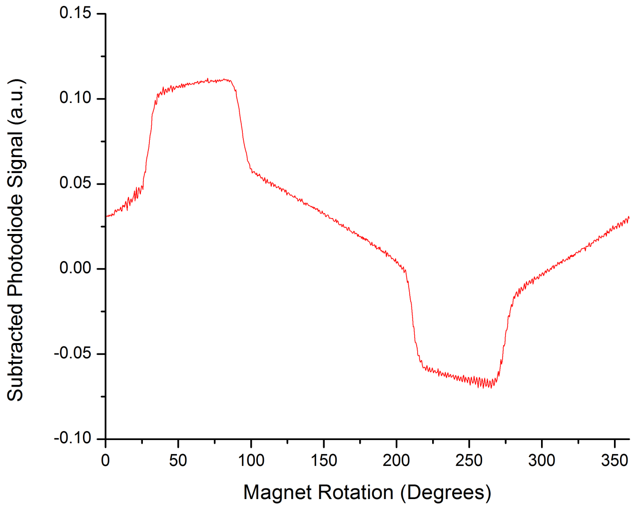

Figure 2.4: Magnetic hysteresis measurement of LuIG done using MOKE. The abrupt changes in output signal correspond to magnetization pinning at an easy axis in the system. This behavior demonstrates complicated crystal anisotropy.

in further experimentation.

2.2.2 Sample Preparation for Bulk Magnetic Characterization

The samples of both LuIG and YIG were grown by liquid phase epitaxially(Ilyashenko Group Moscow State University and Shin-Etsu Chemical Co. ltd.). The LuIG substrate was a layered thin film with an aluminum layer on top for protection. The structure consisted of a 3 μm layer of LuIG on top of a thick ($\sim$100 μm) layer of Gadolinium Gallium Garnet (GGG) which is paramagnetic, transparent, and atomically matched to the LuIG layer. Similarly the YIG sample consists of GGG substrate layer with (110 ± 5 μm) of epitaxially grown YIG on either side. This can be seen in figure 2.6, which is an SEM image of the side profile of a small section of YIG showing the different layers.

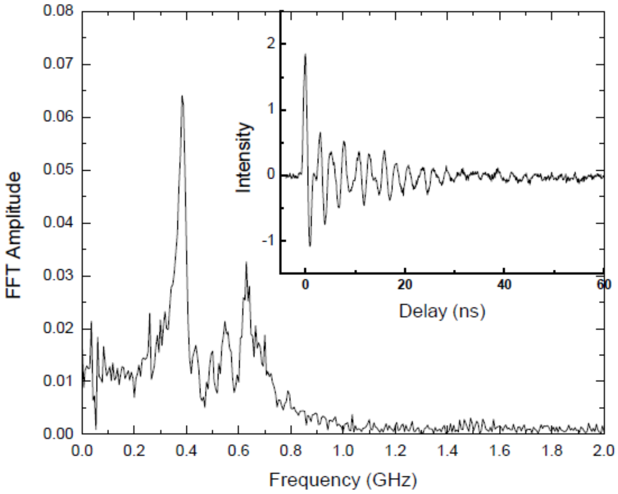

Figure 2.5: FMR measurement of LuIG (inset) with the corresponding FFT of the data. As can be seen there are some sharp peaks corresponding to specific frequencies of FMR with the main peak residing at ∼350MHz. This data was provided by Alastair Fraser.

The method of measuring the magnetic behavior of bulk material used was the Faraday Effect which relies on changes to polarized light passing through the magnetic medium, and will be further described later. Due to the need for the light to pass though the material preparation was needed to ensure the samples were transparent to the laser light.

The LuIG sample was received as a 3 inch wafer, which was then diced by Alastair into smaller segments. To ensure minimal material loss, pieces 1×2 mm were first used. These proved to be too complicated to handle for polishing, and segments of 1×1 cm were used instead. To eliminate the aluminum coating a simple etch was used (16:1:1:2 solution of Phosphoric Acid, Nitric Acid, Acetic Acid and Water). Once the material became transparent it could be safely assumed that the aluminum coating was removed. With the LuIG layer being 3 μm thick no further polishing was needed to ensure transparency to the laser light, as the GGG layer is clear.

The YIG sample was similarly received as a 3 inch wafer, which was also

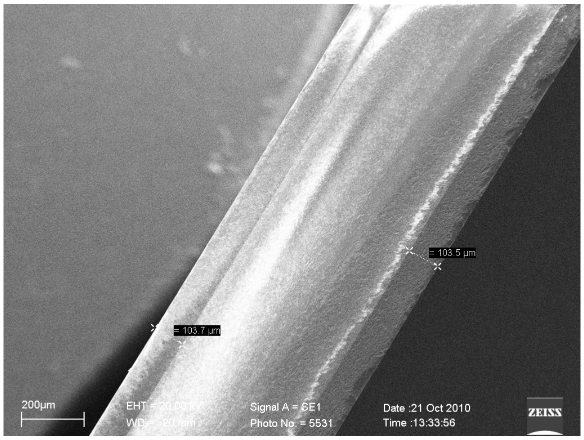

Figure 2.6: SEM image showing a cross-sectional view of the layers of YIG surrounding a GGG handle layer.

diced by Alastair. With no coating, only a cleaning was required in a quick acetone isopropanol (IPA) water process. Since the YIG layer was ∼100 μm thick and on both sides of the material, polishing was needed to allow light to pass through. This was done using 20 μm, 3 μm, 1 μm, and 0.5 μm grit diamond abrasive in reducing order. The sample was mounted onto a flat aluminum stub that was cleaned with IPA. This mounting was done using a wax that dissolves in acetone to allow easy removal. To mount using the wax, a small fragment was placed onto the aluminum stub, which was heated to ∼ 150°C causing the wax to melt. The stub was then removed and placed on a cooling block, while a clean glass microscope slide was used to spread the wax into an approximately equal layer. The sample was then placed onto the wax and gently held in position by teflon tipped tweezers. Once cooled the sample was moved to the polishing stations which was prepared with a 20 μm diamond abrasive sheet. With a steady flow of water to remove debris from the polishing pad, one of the YIG layers was completely removed, which can be determined from a visual inspection under a low powered optical microscope as a color change in the material. The sample was then removed by heating and then using an acetone bath followed by dipping in IPA to remove acetone residue, and was remounted with the remaining YIG side facing up. Using a 3 μm followed by a 1 μm grit the sample was polished until a color change started to appear. With the sample being semi-transparent in white light, it was deemed adequate for using the MOKE setup. A final polishing was done with the 0.5μm grit abrasive to ensure a smooth surface and the sample was once again removed.

2.2.3 M-H Hysteresis

To allow MOKE to be performed on the samples, they required mounting in a way that allowed light to pass through them unobstructed. To assist in this a special mount was made using metallic clips to hold the sample in place. This allowed the wafers of material to be mounted in the sample position in figure 2.7. With the samples mounted, the rotating permanent magnet was used to apply a directionally varying magnetic bias. With a single polarization of laser light passing through the sample and interacting with the spins through the Faraday effect, a rotation in polarization occurs. The beam is then passed through a Glan Thompson crystal and each polarization is measured in a separate photo diode. By calibrating the light so that the signal from each photo diode is equal before the measurement is taken, comparisons can be made between different samples on the same setup.

With the LuIG sample mounted, hysteresis were measured for near and far magnetic fields. This can be seen in figure 2.8(a), which shows the hysteretic behavior of the in plane magnetization of the sample. The noticeable steps in the magnetization curve indicate an easy-axis due to crystal anisotropy, which is non-ideal for vortex or domain wall propagation measurements. With an easy-axis alignment direction, combined with inducing further shape anisotropy through milling, the LuIG proved to be a poor choice

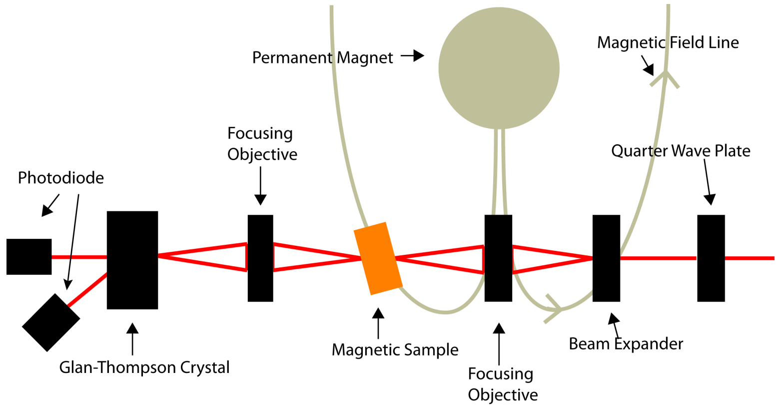

Figure 2.7: Schematic of M-H Hysteresis Measurement Setup, The system involves passing polarized light through a sample with an AC bias field applied. This signal is measured as a change in polarization at the photo diodes.

of material. This lead to a thorough study of the YIG sample, neglecting the LuIG in further measurements. As can be seen in figure 2.8(b), the YIG sample shows a clean sinusoidal curve in the high field and low field scans. This is an indication of no noticeable shape anisotropy in the signal, as the magnetization follows the permanent magnet without "sticking" to any specific directions. With fewer concerns about anisotropy, the YIG was chosen for further experimentation.

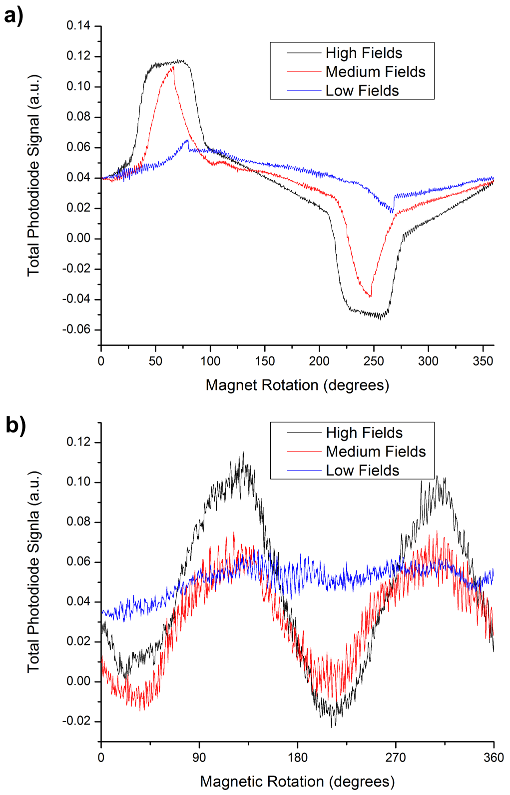

Figure 2.8: Magnetic Hysteresis Curves Showing a) LuIG in high, medium and low fields, b) YIG in similar fields. As can be seen the YIG shows a sinusoidal curve, implying that there is no pinning of the magnetization, where as the LuIG shows clear jumps in signal corresponding to un-pinning.

2.2.4 Sample Preparation for FIB Milling

The next step towards torque magnetometry and possibly magneto-mechanical coupling of the YIG sample involved shaping in the FIB, which meant that the sample required further preparation. A new 1×1 cm sample of YIG was prepared, except with the intent of creating a clean 90° edge for milling. This required the sample to first be polished flat on the thin wafer edge to remove sharp features and roughness left behind by the dicing saw. Using a Model 590 Tripod Polisher the sample was mounted using wax and carefully polished to a flat level surface with $3\,\mu$m, $1\,\mu$m, and $0.5\,\mu$m grit diamond abrasive in reducing order. Once polished, the sample was switched back to its flat surface, and the 100 μm thick YIG layer was carefully polished to ensure a clean 90° edge. Inspection was done under an optical microscope during the process to ensure the sample was polishing at a consistent rate. Once polishing was finished, the sample was cleaned in an acetone-IPA-water process to remove any leftover residue and ensure a clean surface.

Since the FIB involves a highly charged beam of ions as well as constant SEM images involving further charge, the insulating garnet required a layer of material to alleviate these charging effects. Using a Denton Desk V Sputtering system a $\sim$5 nm carbon layer was deposited on the surface of the YIG. By doing so, charge build up on the sample has a path to escape, which was helpful for not only imaging, but many other aspects of the process. With enough charge the sample is able to drift slightly with respect to the FIB column, leading to blurred out features being milled. Also when using a micromanipulation probe, charging to the sample can lead to movement and possibly destruction during the releasing of a device.

With a layer of carbon on the sample, it was placed in a specially designed mount using a set screw to avoid issues with bonding agents. The design of the sample holder by Dr. Douglas Vick allows for the YIG to sit at any angle needed using a specialized set of FIB mounts, with the highest point in the system being the edge of the YIG to be milled. An image of the sample in this mount can be seen in figure 2.9 demonstrating the easy access to the milling edge. With the sample mounted the YIG was ready for further milling into a disk shape for torque magnetometry.

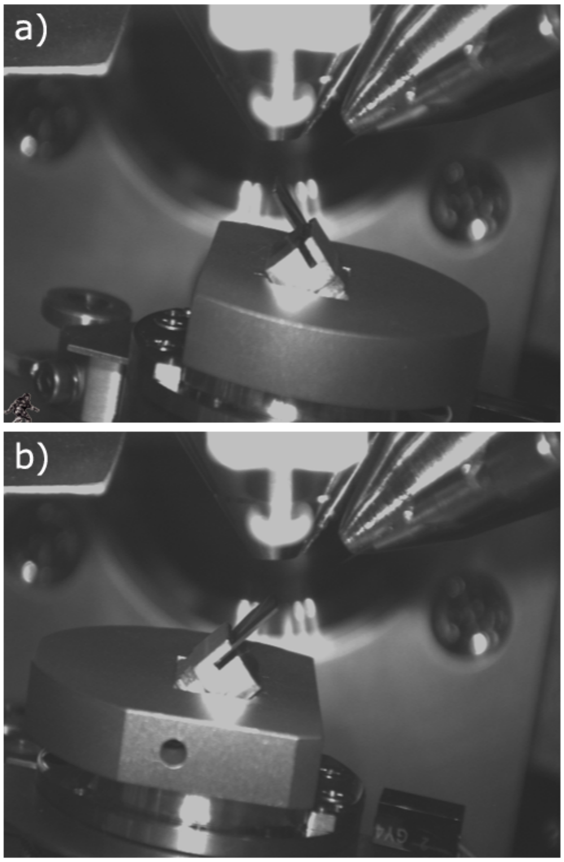

Figure 2.9: SEM image of YIG segment mounted on a specially designed sample mount in the FIB chamber. (a) and (b) show how the mount allows for easy axis to both faces of the YIG segment.

2.2.5 FIB Milling of a Micromagnetic Disk

When designing the shape of the magnetic material for torque magnetometry many properties were taken into account. By using known saturation magnetization supplied by Shin-Etsu ($M_s = 141.6\,\mathrm{kA/m}$) and assuming zero sample anisotropy, a micromagnetic simulation was done by Jacob Burgess in our group using a Landau-Lifshitz-Gilbert (LLG) micromagnetic simulation package. With known achievable size constraints from the FIB, a disk of YIG with a diameter of 700 nm and a thickness of 300 nm was simulated and shown to support a vortex like state. This evidence provided a good indication of the capabilities of YIG for vortex support, which motivated an attempt to re-create the disk shape in the FIB, and to place the element onto a resonator for experimental torque magnetometry studies.

By using the previously mentioned prepared YIG sample in the FIB holder, an attempt was made to mill a membrane, which could be shaped and manipulated. To first judge the milling time needed, silicon was chosen in the FIB settings as the milling material, and a milling for two separate depths was done. These showed that the YIG mills in a similar manner to silicon, with about half of the speed. Using this information and a 6.5 nA current probe, a large trapezohedral trench was milled into one edge of the YIG sample, sufficiently deep to allow blow-out of material when milled from the connecting edge. This was followed by scoring of the edge of the sample to allow alignment when turned 90°. With alignment marks milled into the edge, the sample was rotated and a second connecting trench of similar shape was milled. The resulting structure was a suspended bar, which is easily accessible from both edges of the sample and can be thinned into a sufficiently thin membrane. This can be seen in figure 2.10, which shows the sequence of milling for the trench.

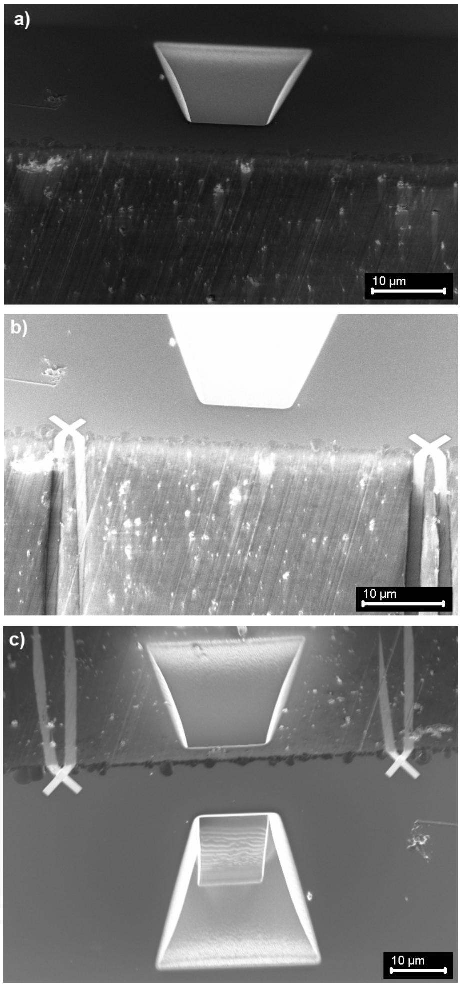

Figure 2.10: SEM image sequence showing the milling of the trench in YIG. (a) Shows the initial trapazohedral hole, followed by scoring marks being added in (b). (c) shows the final suspended membrane with two connected trenches.

With the membrane of YIG suspended, a thinning was done to the appropriate thickness. This step was especially prone to non-planer milling due to the Gaussian profile of the gallium beam. To alleviate some of these issues smaller currents were used for longer periods of time until a mostly planer membrane was fabricated. Using the micromanipulation probe in the FIB combined with an organo-metallic gas containing platinum ((Trimethyl)methyl -cyclopentadienylplatinum(IV)) an attempt to remove and manipulate a segment of the membrane was made. To assist in this process a "finger" of YIG was milled from another section of the sample to allow attachment to the micro-manipulator causing a more well defined point for careful attachment to the YIG membrane. The idea was to ensure that the manipulation probe tip was attached at the lowest point to the membrane segment of YIG, as to not make contact on the eventual resonator platform when placement was made. The finger was attached to the probe carefully using FIB and SEM images as guides and a rectangular section of the membrane was carefully removed and lifted away from the substrate as seen in figure 2.11.

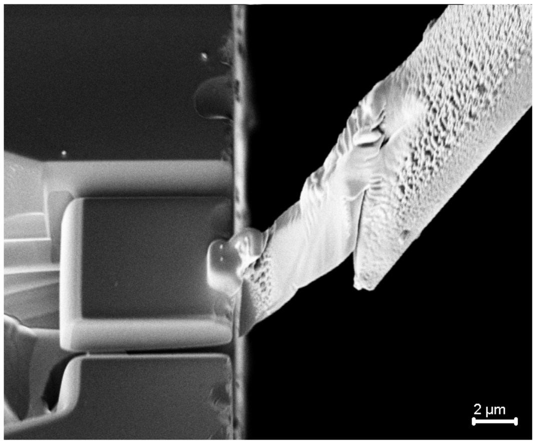

Figure 2.11: SEM image of a rectangular membrane of YIG attached to a small finger, which is consequently attached to the FIB manipulation probe. All of the attachments were done using platinum deposition in the FIB.

To ensure that once a disk was cut it could be bonded sufficiently to a membrane, the unshaped segment was first tried. A $100\times100\,\mu m$ silicon nitride membrane (100 nm thick) was loaded into the chamber with the YIG segment still attached to the probe. A rectangular section was cut into the membrane to further ensure that the probe did not make contact, which might cause destruction of the membrane. The probe was then carefully aligned with the membrane, in a similar manner to the finger, until contact was made. This was followed by bonding of the YIG segment to the membrane using a thin layer of platinum with the SEM supplying the ionizing energy needed for the gas to bond. To release the probe, a low current cut was made across the joint between the finger and the YIG segment. During this cut the membrane was destroyed due to charging effects, along with the force generated by releasing the probe under tension. Although ultimately unsuccessful, this provided needed alignment practice as well as showing that bonding was possible.

To shape a disk, a YIG membrane was made in a similar manner to figure 2.10. The probe was once again attached to a rectangular section of the membrane (without a finger) and a segment was released. While suspended the rectangular segment was shaped into a crude disk with a tab. Due to the fact the regular FIB control software only allows straight edges and single burn spots, the shape of the element could only be approximated. This left very sharp features on the edges of the disk, which is problematic for magnetic measurements due to vortex nucleation and pinning in the material. An image of the resultant disk shape can be seen in 2.12(a). An attempt was then made to place the disk onto a silicon nitride membrane to allow a resonator to be milled around it. Due to a vibration of the system associated with reaching the extremities of the controlling piezo, the sample was destroyed in the process.

Pre-designed and released silicon paddles were chosen to be used as the device platform for the next trial, as they have been shown to have very well defined characteristics for torque magnetometry[31]. A circular paddle design was made in the RAITH to allow a clean paddle to be sculpted, as can be seen in figure 2.12(b), and a membrane was defined in the usual manner. The disk was cut into the membrane once it had reached an appropriate thickness (figure 2.13(a)) and the manipulation probe was attached (figure 2.13(b)). With the silicon paddles loaded in the chamber a channel was milled into the substrate to allow the probe room to touch down. The disk was then carefully

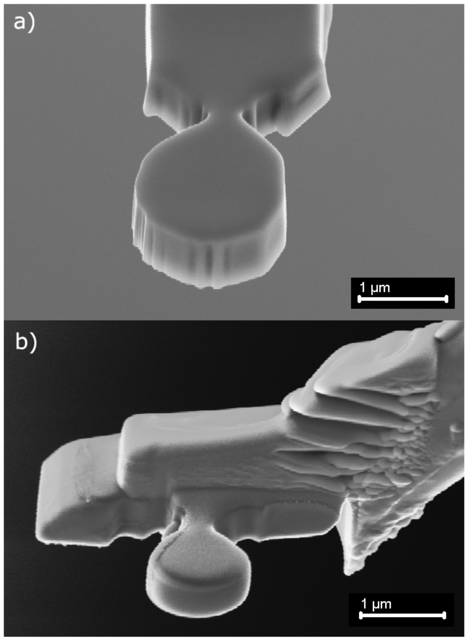

Figure 2.12: SEM image showing a comparison between YIG disks milled with (a) straight cuts and burn holes, and (b) using RAITH software

moved over the paddle and placed in contact, which was seen as a deflection of the paddle (figure 2.13(c)). Bonding was done using platinum followed by a retraction of the gas injection nozzle. Upon the retraction vibrations in the system caused the sample to release from the probe leaving the device intact (figure 2.13(d)). Although the device was largely fine, a nano-crack was induced in one of the torsional bars leading to a need for repair. This repair was done once again using a platinum deposition, leaving a working device with a magnetic YIG disk placed on it.

2.2.6 Silicon Paddle Mechanical Characterization

With a shaped magnetic element placed on a working torsional resonator, frequency response measurements were carried out by Joe Losby. The measurements, done using optical interferometry, can be seen in figure 2.14, showing the response of both the YIG paddle and a bare paddle. Both paddles were

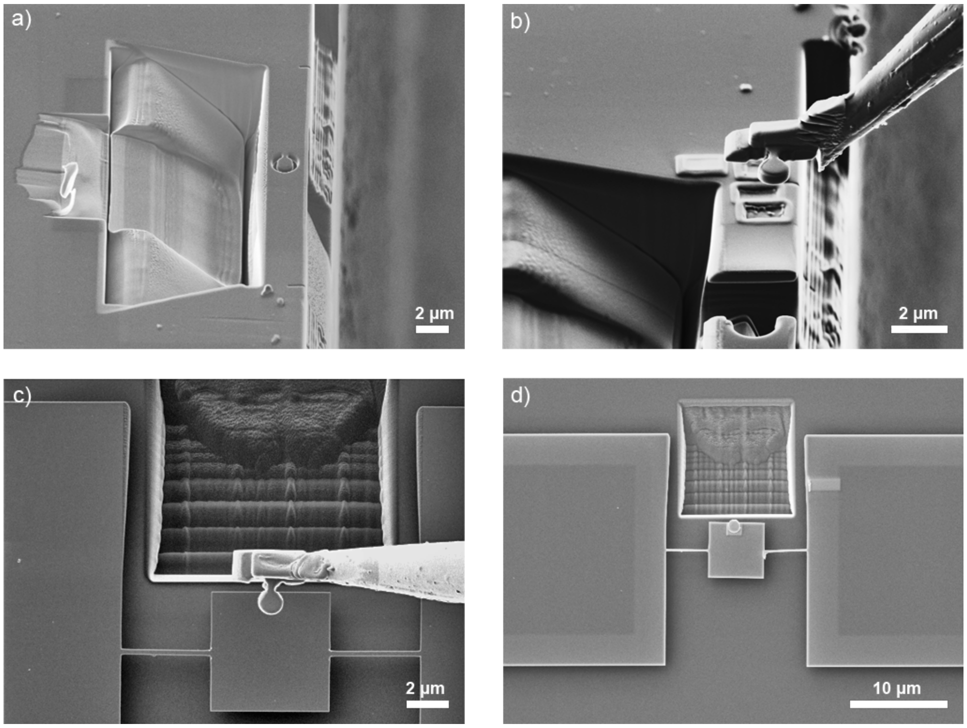

Figure 2.13: SEM image sequence showing the sculpting and placement of a YIG disk onto a silicon paddle torsional resonator. In this figure (a) shows a freed YIG membrane supported across a blow-out hole with a small disk milled into it, (b) follows with the FIB micromanipulation probe attached to the membrane stiction containing the disk, (c) is a top down alignment image showing placement of the disk onto the resonator, and (d) shows the final working device after releasing the disk.

actuated magnetically using an out of plane dither modulated by an AC current pulse[3]. This actuated a resonance in the device which was picked up by a modulation in transmission, due to interference with a optical beam reflecting off of the base silicon dioxide layer. With the lock-in amplifier both generating the signal and measuring the response, frequency response profiles could be made for both the YIG and the bare paddle. These profiles show the first out of plane mode of the resonator along with the first torsional mode, which is the mode of interest for our purposes.

As can be seen in figure 2.14(b)(inset) a well-defined thermomechanical

---

[3] The bare paddle could be actuated due to a paramagnetic effect of material present after the reaction of the gallium with the organometallic precursor gas

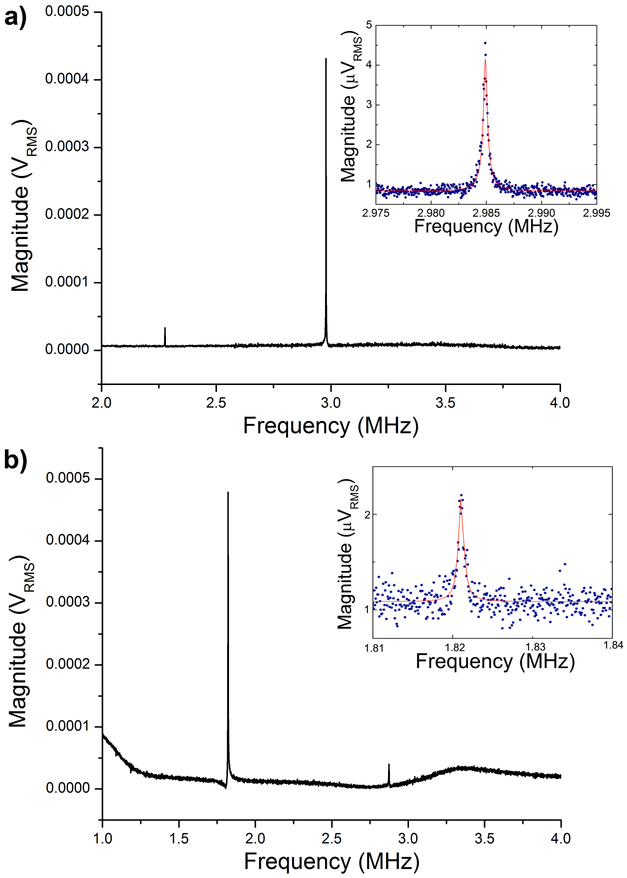

Figure 2.14: Data showing the frequency response of (a) a bare silicon paddle and (b) the YIG disk on a silicon paddle. The large peak in each corresponds to the torsional mode, which is known to be preferably driven in the actuation scheme used, and the small peaks are other unknown modes of the resonator. The insets show the thermomechanical response of each torsional mode. Data supplied by Joe Losby.

resonance peak is observed at the torsional frequency of *1.82MHz*, with a mechanical quality factor $Q = 2660$. This shows a 70% reduction in Q from a bare paddle on the same chip figure 2.14(a)(inset), with a frequency down shift of 35%. To understand these effects, simulations were done using COMSOL finite element modeling software. The paddle was simulated first in its untouched form, followed by the paddle with a disk of YIG of the same dimensions as in experiment, and finally the break in the torsional rod was simulated with and without a platinum bond holding it together. The results of these simulations can be seen in table 2.1, which shows a significant downshifting trend at the mass is loaded on and the break in introduced. When simulating the gap with platinum, it was assumed that the platinum could not diffuse into the gap due to size constraints, with the thickness of platinum used being 20 nm as estimated from SEM images(figure 2.15).

	Bare Paddle (MHz)	Paddle with YIG (MHz)	YIG and Break (MHz)
Torsional	3.78	3.52	2.91
Out of Plane	5.58	5.29	4.57
In Plane	7.28	6.92	5.56

Table 2.1: COMSOL Frequency Downshifting Trends

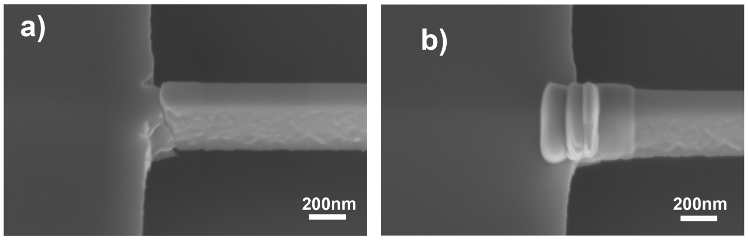

Figure 2.15: SEM image showing a torsional rod break (a) with platinum repair (b), done in the FIB

Even with a break, the paddles in this case proved to be highly sensitive and even capable of resonating due to thermomechanical (TM) noise present in the system. With such high Q paddles, the undriven Brownian motion of the resonators drove the paddles into their preferred resonance, which was measured interferometrically using the lock-in amplifier without a drive signal. These measurements not only proved the capabilities of such devices, but also allowed for a calculation of the torque sensitivity of the devices. Calculations done by Joseph Losby using a torsional spring constant of $3.5{\times}10^{11} Nm/rad$ and a calculated edge deflection of 32 pm showed that the YIG on paddle system had an on-resonance torque sensitivity of $0.16\frac{aN}{\sqrt{Hz}}$, significantly worse than the torque sensitivity of the bare paddle, which was $0.04\frac{aN}{\sqrt{Hz}}$. These results confirmed that the paddle was acting as expected, allowing magnetic analysis to be carried out confidently.

2.2.7 Silicon Paddle Torque Magnetometry

With the mechanical properties of the paddle known, torque magnetometry measurements were carried out on the disk by Joe Losby. Due to geometrically induced shape anisotropy a vortex like state was supported in the disk. This vortex was then forced across the length of the disk by applying a large bias field, until it annihilated at an edge. By pulling the vortex across the disk, and applying an out of plane dither field of ~ 0.15 kA/m, a localized mechanical torque was caused which was seen in the frequency response of the paddle. Measuring the frequency response with an interferometric lock in system, similar to what was used in the mechanical characterization measurements, allowed a probe or the local energy landscape in the path of the vortex. Figure2.16 shows the response of the paddle with an induced vortex. As can be seen the vortex annihilation and creation cause abrupt steps in the mechanical response of the system, showing a well defined state. The inset to figure 2.16 shows a comparison between the response of the YIG disk to the response of a Permalloy disk deposited on similar silicon paddles. As can be seen, the Permalloy shows many abrupt steps in the signal, corresponding to Barkhaussen-like steps. These are caused by pinning of the vortex at local defects such as crystal boundaries, which is why the epitaxially grown single crystalline YIG shows a much cleaner signal. This proves the major advantage to the process of FIB milling and placing epitaxially grown magnetic materials onto paddle resonators.

Finally to ensure that the magnetic states seen in experiment actually corresponded to a vortex, detailed simulation were carried out by Jacob Burgess

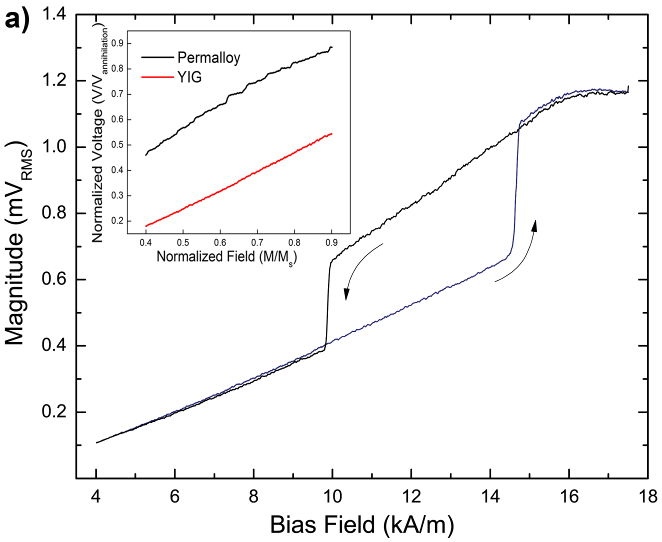

Figure 2.16: A magnetic hysteresis curve of the YIG disk measured at room temperature using a silicon paddle torque magnetometer. The inset is a comparison of epitaxially grown YIG to Permalloy, showing the lack of pinning in YIG.

in LLG of the exact disk used, using measured dimensions. By applying energy to the system and allowing the disk to relax into its ground state, it was seen that a three dimensional vortex was supported. Images from these simulations can be seen in figure 2.17, which show the football like vortex in the bulk of the disk. The surface state looks similar to the usual one dimensional vortex cores seen in Permalloy, with the magnetization of the disk rotating around the core, but when looking at the cross-sectional view, the multidimensional shape of the disk is apparent. Although the vortex is non-ideal, it still allows a probe into the local energy landscape of the disk, making this technique useful for detailed magnetic studies.

2.3 Conclusion

A section of epitaxially grown thin film YIG was polished, shaped and then milled using a FIB. By referring to micromagnetic simulations of micro-disks

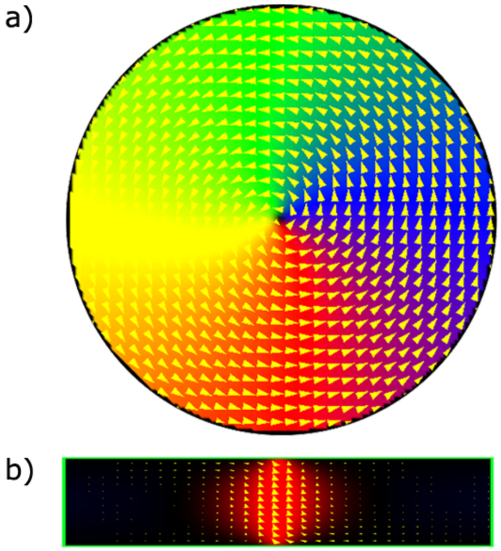

Figure 2.17: Micromagnetic simulations of the vortex state in a YIG disk of the dimensions fabricated. Part (a) shows a top view, with the color showing the direction of the magnetization at different points in the sample. This shows a vortex core in the center of the disk. Part (b) shows a side view of the same simulations, giving indication of a 3-D vortex like state through the bulk of the disk. Simulations were done by Jacob Burgess using LLG.

made of YIG carried out by Jacob Burgess, the dimensions of the disk were chosen. The process of milling was refined until an appropriate shape was made with as much precision as allowed, followed by a careful manipulation onto predefined suspended silicon torsional resonators. The characterization of these resonators was done mechanically by Joseph Losby showing normal resonant behavior. This was further studied using finite element simulations, which gave insight into the effects of a small break of the torsional rod and repair using platinum gas. Torque magnetometry was performed on the system, showing the creation and annihilation of a vortex state, which was further supported by more detailed micromagnetic simulations. These measurements also demonstrated the advantages of using single crystalline material, as the signal was shown to be much cleaner than that of a Permalloy disk, with no noticeable Barkhausen-like steps in the magnetization.

The experiment was deemed an overall success as a platform to study micro- and nanomagnetic effects, isolated from bulk systems, on very pure samples. This demonstrates a potential for measurement on further systems including magnetic islands[63] and multi-ferroic materials[64]. By allowing placement of such pure and well behaved materials one is able to study magnetic effects that would normally need to be simulated, in a much more reasonable time scale and a much more realistic system.

Chapter 3

Photonics

This chapter covers the design, fabrication, and testing of a photonics based NEMS for the purpose of magnetic sensing. Design and simulations were done using finite difference time domain (FDTD) methods to understand light propagation in the system. The results from these simulations as well as the process from design to testing is outlined, and a working device is demonstrated.

3.1 Intro

3.1.1 SOI Photonics for NEMS

Silicon on insulator architectures provides an ideal platform for photonics for many reasons[65]. The main one of these being the fabrication methods available due to advancements in the semiconductor industry. By utilizing older industry technology, photonic elements on the hundreds of nanometers scale can be fabricated with minimum surface roughness to allow very low loss elements[66]. Having exact control over the spacing and sizing of elements and still being able to produce many at a high rate is crucial to the prototyping world of research. By doing so it is allowing hundreds of device iterations to be done in a cost effective manner, without the time and effort needed for many other fabrication techniques [67, 68]. This gives the ability to study and fine tune selected components of the systems until the improvement of the overall device surpasses that of a non-photonic based equivalent.

The key to photonics is the ability for light to couple and transfer between different elements. By doing so one can create isolated cavities, whether it is in a photonic crystal lattice [40, 69] or a ring structure [70], to amplify and guide the light. This stems from the fact that similar to electrons in a potential well, there exists some amount of light outside of defined waveguides. Due to the fact that the modes supported in the waveguides are Gaussian in nature, they decay rapidly from the central maximum but exists in small amounts far from this peak. The light that is leaking is refereed to as the evanescent tail of the Gaussian beam, and decays exponentially away from the waveguide. This can be visualized in figure 3.1, which shows a diagram of a Gaussian mode propagating in a waveguide.

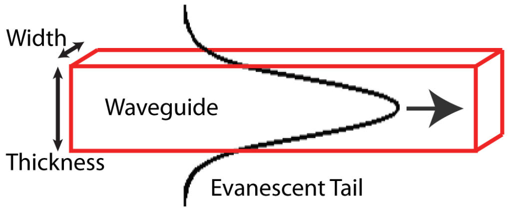

Figure 3.1: Schematic of a Gaussian mode propagating in a waveguide, which shows the leaking evanescent tail region.

With this tail existing outside of a waveguide, the light is able to reach a second waveguide, placed in close proximity, and some of that energy can transfer. After some length the light will eventually fully leak into the second waveguide, creating a propagating mode, and leaving the primary waveguide completely empty. This transfer is the key to creating cavities for light amplification, as the cavities parameters can be tuned in such a way to allow the light to build up without leaking entirely back into the primary waveguide[71]. This entails creating a cavity with the total circumference being an integer number of wavelengths, for whatever operating wavelength is chosen. By utilizing the these cavities, the power can be amplified. When this is then combined with a NEMS device, it can yield increased sensitivity. Optimizing systems has the potential to result in devices more sensitive than current technologies, which can be integrated into electrical systems and lab on a chip schemes more easily.

3.1.2 FDTD Simulation Background

Since 1966[72] FDTD simulations have given a method of calculating the propagation of electromagnetic waves in a medium. Although merely proposed in 1966 by Yee, the methodology proved to be very robust in its nature, allowing for massive simulations of all types of phenomena. The actual term FDTD was later coined by Taflove[73] when he applied the method to a steady state electromagnetic wave. Since that time, it has become commonplace to use this method in photonics[74], plasmonics[75] and other fields of research[76]. This is due to the fact that dividing a region of space into gridded cells (Yee Cells), and numerically solving for Maxwell's equations gave accurate and calculable results for systems early on. The finite difference term arises from the use of the central difference approximation of the Maxwell derivatives between cells to solve for the fields at a point in time. The time domain component comes from the fact that the wave is calculated propagating in time, which allows for a broad frequency range to be easily calculated.

To understand how this method works numerically a Yee cell is needed. figure 3.2 shows a diagram of such a cell. This diagram shows how a section of space is divided into a grid of cells, with the electric (E) fields being calculated at points in the middle of the edges, and the magnetic (H) fields being calculated at the central normals to the faces of the cube[72]. This allows the magnetic field at each point to be calculated from the surrounding electric field components, and vise versa, using the finite difference method. The calculation then moves forward for the next instance of time, propagating the electromagnetic field by continuously solving.

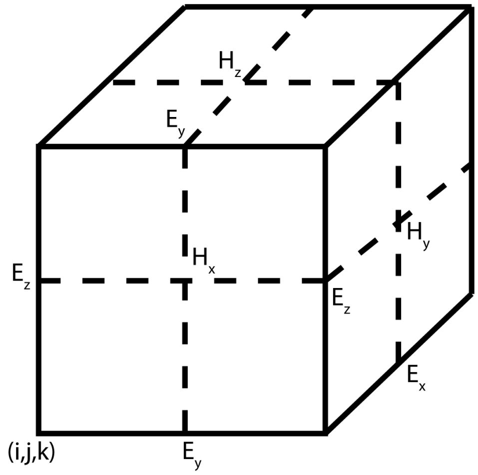

Figure 3.2: Diagram of a Yee cell, showing the points at which the electric and magnetic fields are calculated.

FDTD solves the discrete version of the Maxwell's curl equations which can be seen as follows:

$$H^{n+1/2}_{x(i,j,k)} = H^{n-1/2}_{x(i,j,k)} + \frac{\Delta t}{\mu \Delta z}(E^{n}_{y(i,j,k+1)} - E^{n}_{y(i,j,k-1)}) - \frac{\Delta t}{\mu \Delta y}(E^{n}_{z(i,j,k)} - E^{n}_{z(i,j-1,k)}) \tag{3.1}$$

$$E^{n+1}_{x(i,j,k)} = E^{n}_{x(i,j,k)} + \frac{\Delta t}{\varepsilon \Delta y}(H^{n+1/2}_{z(i,j+1,k)} - H^{n+1/2}_{z(i,j,k)}) - \frac{\Delta t}{\varepsilon \Delta z}(H^{n+1/2}_{y(i,j,k+1)} - H^{n+1/2}_{y(i,j,k)}) \tag{3.2}$$

In these equations E and H are your electric and magnetic fields respectively, (i,j,k) refers to your position on the Yee grid, $\Delta t, x, y, z$ are the infinitesimal steps in time and space, and μ and ε give your permittivity and permeability in the material. By calculating one of the field components and then moving forward by a half time step to another grid point (known as the leapfrog method), the fields can be calculated for the entire grid numerically. This works well for many variations of elements but only if the dimensions of the element are on similar scales. This is due to the fact that a very long and thin object, such as a wire, requires and enormous number of grid cell to calculate. Also to ensure that the calculation will eventually converge, a perfectly matching layer (PML) can be used at the boundaries of the grid. This causes no reflections to occur, which would re-introduce radiation into the system and cause the calculation to continue, resulting in numerical artifacts.

By including an initial source of electromagnetic radiation, and using the leapfrog method to determine the electric and magnetic field components at all point in space for a set time, a continuous wave can be numerically simulated. This wave can propagate and interact with other materials, allowing a study of how photonic components work, which can greatly assist in device design and fabrication.

3.1.3 Photonic NEMS Detection Background

Detection of NEMS in photonic systems is based on modulations of the effective index of refraction as seen by the propagating mode. This stems from modulation in spacing between the mode and surrounding substrates, due to the fact that the evanescent tail exists far outside of any defined waveguide. By a mechanical modulation of a NEMS, acting as a waveguide, the speed of light in the medium slows down or speeds up depending on if the index becomes higher or lower. This means that the time it takes for light to travel through the waveguide depends on the waveguides spatial position during an oscillation. By measuring this output modulation of the phase of the light, the frequency of mechanical resonance can be obtained. To further improve upon this method, one can embed the NEMS in a very high optical Q cavity. These cavities, such as a ring resonator, work by meeting a periodic boundary condition, which causes them to only allow a very small bandwidth of light to propagate. Accepting only certain frequencies, leads to a very sharply peaked spectrum, where the peak separation is known as the free spectral range (FSR), which is governed by the following equation representing a Fabry-Perot analogous equivalent to a ring resonator system:

$$\Delta\lambda = \frac{\lambda_0^2}{2nlcos\theta + \lambda_0} \approx \frac{\lambda_0^2}{2nlcos\theta} \tag{3.3}$$

Where $\Delta\lambda$ gives the spacing between adjacent peaks, λ_0^2 is the central angle of the nearest peak, n is the index of refraction, l is the length of the cavity, and θ is the angle of incidence of the light into the system, which has no equivalence for the ring resonator system. From this equation it is possible to solve for the length of cavity needed to allow propagation of certain frequencies of light, or conversely what frequency of light will propagate in a certain length of cavity. The result of this manifests itself in a spectrum with several sharp peaks, spaced apart according to the index of a material and the cavity length. By modulating the light in a cavity of this nature, the FSR shifts slightly. This is illustrated in figure 3.3, which shows how the peaks modulate. By choosing a frequency that corresponds to a steep slope, a very small modulation of the FSR can lead to large modulations of the output signal. Using this premise, small mechanical modulation can be detected photonically, leading to very high sensitivity measurements.

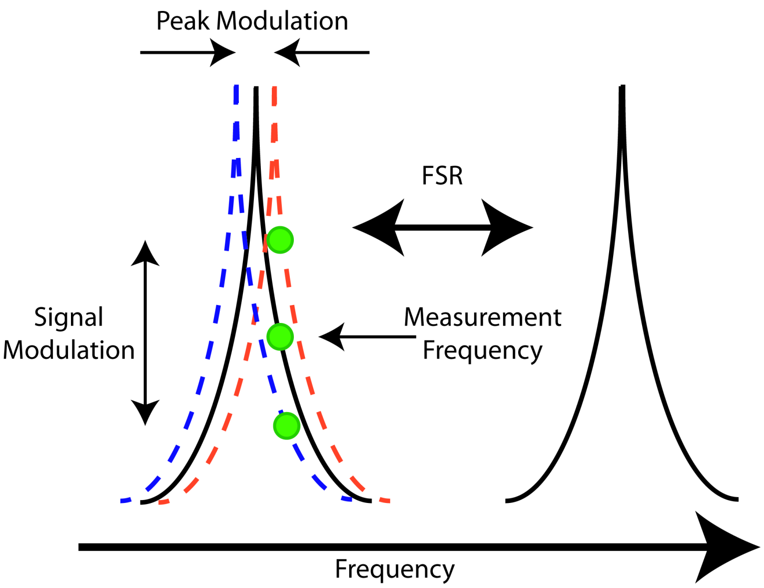

Figure 3.3: Schematic showing the free spectral range oscillation due to mechanical movement. As the peak oscillates, the signal at the point of measurement changes proportional to the slope of the peak.

3.2 Experimental

3.2.1 Motivation for using NEMS in Photonics

With NEMS providing an excellent platform to measure micro- and nanoscale properties of materials, there has always been a large focus on improvement. As discussed in the introduction to this thesis, this can include scaling of the device, improvements in transduction methods, and improvements in detection. By utilizing integrated photonics, the latter two of these can be achieved. With most photonics based around the telecommunication industry, which uses a transmission wavelength of 1550 nm, the obvious choice for a device was to use SOI architectures. This is because these types of materials are well studied, CMOS compatible, and propagate light at 1550 nm with low losses. Since knowledge in my research group at the time was limited in this field, and competing research groups such as Tang *et* al. were rapidly producing devices[77], the drive to learn about integrated photonics was very high.

To help understand and model such systems, a course was taken at the University of British Columbia, in part with Microsystems and Nanotechnology Group (MiNa) and CMC Microsystems. This allowed access to fabrication facilities at IMEC using CMOS capable photolithography to create a plethora of devices, as well as FDTD software supplied by Lumerical Solutions Incorporated. Using the FDTD simulations as well as known parameter constraints from IMEC, designs could be modeled in full to allow the creation of silicon based photonic devices.

3.2.2 Effective Index Study of Silicon

With a NEMS system in mind, the final device design was guaranteed to include several elements such as grating couplers, waveguide to waveguide coupling, ring resonators, and photonic crystals. These elements all being critical to making robust devices with high optical Q cavities. To study these elements in detail the effective index method was used. With a silicon on insulator architecture, there are three very different refractive indices at play. The S_iO_2 layer underneath the silicon and the air layer on top have significantly smaller indices of refraction than silicon ($n_{S_iO_2}$ =1.527, n_{air}=1.000, n_{S_i}=3.477)[38]. When this is combined with the fact that a propagating mode has an evanescent tail residing outside of the silicon layer, the indices of these outer materials must be taken into account to accurately model the mode. The effective index method can be used to avoid doing large 3D simulations, which are time and resource consuming, by using averaging. To account for all of the different indices as seen by the mode, the effective index method represents them as an average effective index across the entire mode cross section. By doing so, a inherently 3D problem can be reduced to two dimensions and become easily computable.

To determine the effective index of a silicon strip waveguide of thickness 220nm and width 500nm, placed onto a silicon dioxide layer of thickness 1 μm, a simulation was done. Figure 3.4(a) shows the geometrical setup of the simulation, including the injection of the light into the waveguide. With perfectly matching layer (PML) boundary conditions chosen, and concentrating on the TE polarization, the mode profile for this system was generated figure 3.4 (b). This profile results in the effective index of the material, which in this case is $n_{eff} = 2.838$. By knowing this effective index value, all of the material in the area surrounding the system can be represented by setting the waveguides as a custom material with an index of n_{eff}.

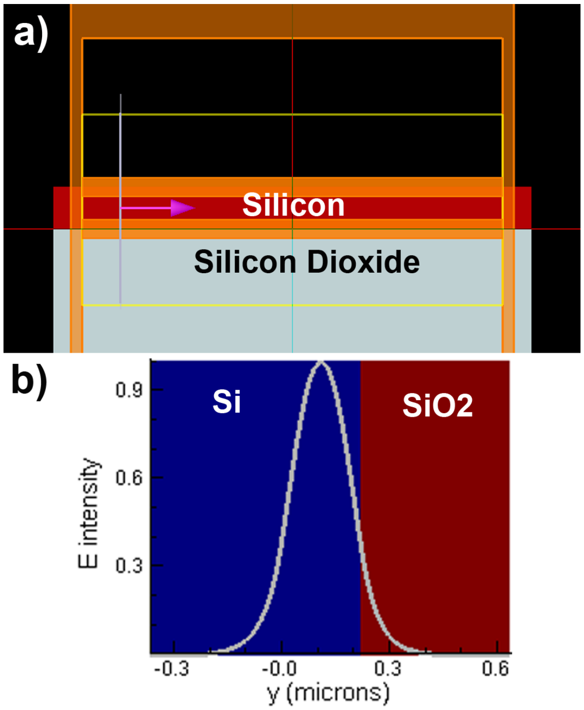

Figure 3.4: Simulation of the Effective Index in SOI Architecture. (a) shows the FDTD simulation layout used and (b) shows the normalized mode profile at the boundary, giving you the effective index of the system.

When considering a mechanically resonating photonic device, the main modulation in signal is a result of the mechanical displacement. As the separation between the waveguide[1] and the underlying substrate changes, the effective index seen by the mode also changes. This causes the light to slow down or speed up depending on the position of the mechanical resonator, leading to a phase modulation of the light, and giving you your transduction scheme. By creating a two dimensional system once again, except including an air gap of a set size corresponding to a mechanical separation, one can look at how the effective index changes with gap size. In this type of system the maximum index change the light sees is at the deepest point in the separation, giving you an indication of the sensitivity needed in measuring equipment[2]. By relying on such a method of transduction, the signal can be modulated without significant losses in power, making it ideal in NEMS sensor applications.

3.2.3 2-D FDTD Modeling of Photonic Elements

To model 3-D systems, a two dimensional version can be used, with a known effective index. This allows a condensed top down view of the system to be made, ignoring the out of plane dimension of the material. The results of such a simulation gives evidence to support element designs, while maintaining low simulation times to allow for large parameter sweeps.

With the 2-D material properties known, silicon waveguides were defined, and systems such as waveguide-to-waveguide coupling were studied. With two waveguides separated by a distance less than that of the evanescent tail, a transfer of energy from one waveguide to the other can occur. By adjusting the spacing between two waveguides in the coupling region, and monitoring the power throughout both waveguides, the efficiency of the coupling can be seen. Using a 500 nm wide waveguide, which is known to support single eigen-

---

[1] This could actually be any photonic element that allows propagation of light.

[2] The sensitivity also relies heavily on how sharp the FSR peaks are, and how much loss the system has, but to first order one can get a feel for the changes with this method.

modes of propagating light[38], the spacing between elements was studied. With step changes of 5-10 nm the coupling was viewed as a relative change in power between the two waveguides. The results of this study can be seen in figure 3.5(a) and (b), showing the power distribution between two waveguide for 155 nm and 140 nm respectively.

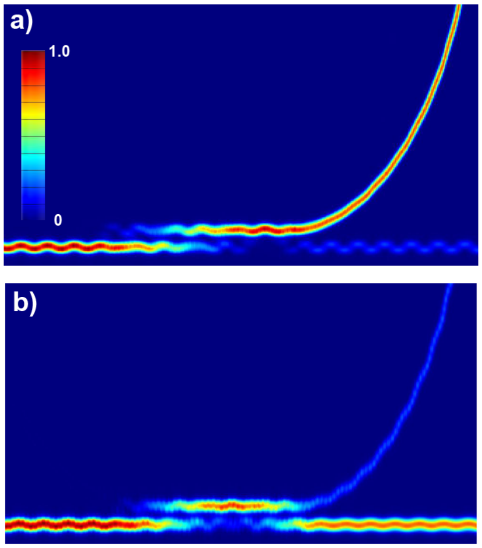

Figure 3.5: 2-D Simulation showing a $10 \times 40 \mu m$ section of the power profiles for waveguide to waveguide coupling with (a) 155nm gap, and (b) 140nm gap. As the light propagates from left to right in the lower waveguide, it is slowly transferred to the upper (curved) waveguide. The color in the plot indicates the power, which was normalized to the input. As can be seen, the coupling is far better for the 155nm spacing.

In this plot the color demonstrates the total power, normalized to the input mode. It is clear from this that there is an ideal coupling separation, for a set length of waveguide, that corresponds to perfect coupling. With the 155nm gap giving near perfect coupling, and the 140nm gap allowing the light to re-enter the original waveguide with very little signal ultimately transferred, the dependence on the separation become obvious. This helps demonstrate the need to model the parameters of such a system to know the expected response without having to fabricate many iterations. If the length or separation of the coupling region is not ideal, the mode can transfer back to the original waveguide or not transfer at all. With the simulation data, as well as restrictions of line widths in the fabrication process in mind, the ideal couple gap was chosen as 150nm for all devices. This allows for the shrinking of the waveguide widths in higher dosages[3], while still maintaining a separation.

With a coupling distance in mind, ring and racetrack resonators were studied. These types of elements are well understood, and can be solved theoretically as seen in the introduction to this chapter. The concept being that if some periodic boundary condition is met, light will be able to constructively interfere with itself causing a build-up of power. Since the properties of these devices arise from periodicity with respect to the wavelength of light being used, and the response of the grating couplers was unknown, minimal simulations were done. The only condition implemented was that the resonators have bending radii of more than 5μm to ensure low losses, and a size large enough to accommodate a photonic crystal element.

3.2.4 Photonic Crystal Design

With an understanding of the transduction scheme in photonic based NEMS, and the sensitivity of torsional based resonators in mind, a photonic crystal was chosen as the key element in the system. Since it has been shown that light can be bent in a photonic crystal at a 90° angle in square lattice designs[78] and 60° angle in triangular lattice designs[79], photonic crystals became an obvious choice to guide light off of the axis of rotation. Forcing the light off of the axis of rotation is needed to ensure that there is a change in separation between the light path in the silicon paddle, and the underlying S_iO_2 substrate, as the paddle oscillates. By causing this oscillation, and ensuring that the separation is not too large, the effective index felt by the light should modulate. Using

---

[3] This will be elaborated upon in section 3.2.6

this knowledge, simulations were done of the 2-D photonic crystal paddle to determine the appropriate parameters for light propagation and bending.

There are four main components when designing a photonic crystal that must be taken into account. These are the lattice separation of holes in the structure (a), the filling factor ($f = r/a$), the size of the line defects, and the number of rows and columns. Knowing that the waveguide leading into the crystal will have a width of 500nm, as well as the fact that the crystal will have to be fairly large to allow maximum deflection of the paddle edges for detection, a triangular lattice crystal with a single line defect was chosen. This corresponded to removing a single row of holes in the crystal where the waveguide met the photonic crystal paddle. Using literature parameters of a filling factor around $f = r/a = 0.30$[79, 80], and an initial radius of the hole elements as $r = 400\,\text{nm}$, a massive parameter sweep was done for both released ($n = n_{S_i}$) and unreleased ($n = n_eff$) devices. From this, data was accumulated by monitoring the power profile across the paddle, an example of which can be seen in figure 3.6. This data allowed the device parameters to be narrowed down to several possibilities for released devices, and unreleased devices, all of which showed some amount of transmission.

To better understand the response of photonic crystals to parameter changes, a comprehensive study was done, following the procedures outlined in [81]. By designing a photonic crystal with 25 rows and 12 columns[4], using a 500 nm waveguide, leading into a single line defect, a full characterization of the change due to varying parameters was made. This was done by sending a pulse centered at 1550 nm into the waveguide and measuring the integrated transmission power at the end of the crystal, normalized to the total integrated power injected into the crystal. First a radius of $0.35a$ was chosen, which was held

---

[4] 25 Rows were used to ensure the boundary effects in the crystal would not be felt by the light.

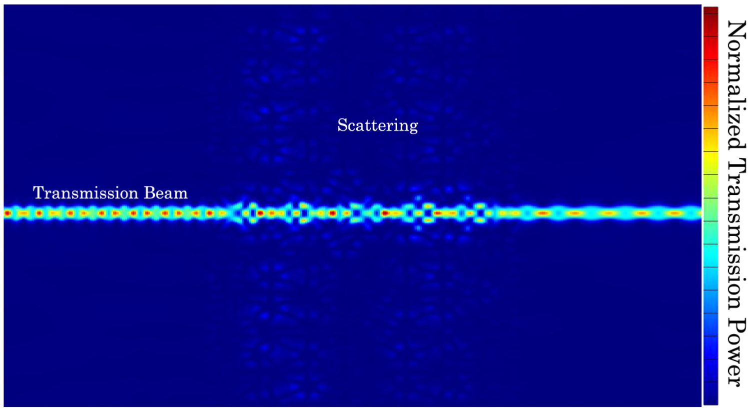

Figure 3.6: Simulation of the power profile through a single line defect photonic crystal. The color corresponds to the transmission power, normalized to the input. Light can be seen passing directly through, as well as scattering off of some photonic crystal holes in the paddle.

constant. A pulse with a frequency range between 1.52-1.58 μm was then injected using specific lattice constant in the simulation. The filling factor was varied between $f = 0.10 - 0.50$ and all the data was compiled in a concise 2-D color plot as seen in figure 3.7.

From this plot, a zone showing maximum transmission can be seen between $f = 0.35 - 0.45$ for almost all wavelengths, with a closer inspection at 1550 nm showing an ideal range of $f = 0.37 - 0.42$. A value in this range, more precisely $r/a = 0.37$, was then used to study the effects of a varying lattice constant. This was done in a similar manner to the study of filling factor above, and the normalized transmission was plotted in figure 3.8. The frequency range in this plot was made significantly larger to show the trends of the parameter variation, with a lattice constant range of 400-1000 nm. This also allowed comparison to the trends seen in [81] for S_iN photonics.

Using the data from all of the above plots, it is clear that if one wanted to make a photonic crystal, with a single line defect, in a triangular lattice orientation, for telecommunications wavelengths, the ideal filling factor would be between 0.37 and 0.42 and the ideal lattice constant would be between

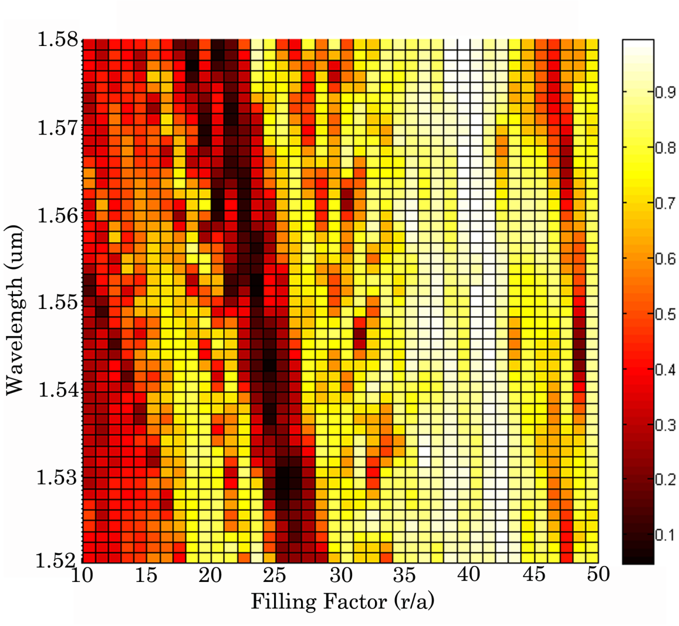

Figure 3.7: Parameter Sweeps for a photonic crystal with a constant hole radius of 0.35a (color showing transmission), showing the acceptance band corresponding to frequency and filling factor variations.

475 nm and 650 nm. The data also gives insight into the variations that can be expected in an ideal system, if fabrication dosages are changed, causing a size scaling of the device.

With the knowledge of single line defect parameters for transmission in a photonic crystal, bending was studied in detail. Since a triangular lattice was used, a 60° bend was chosen as a natural line defect bend in the crystal. To study this, a single 60° bend was designed in FDTD and the transmission was studied in a similar manner to previous simulations. Further research into the design showed that, in order to get better directional scattering at a bend, a single hole can be left with some of the surrounding holes removed. Once the parameters were chosen such that there was light propagation, a complete four bend crystal design was simulated. This can be seen in figure 3.9(a), which shows an FDTD architecture of the 60° bends in a crystal when using a scattering hole. By using this scattering design a mode can be directed at 60°

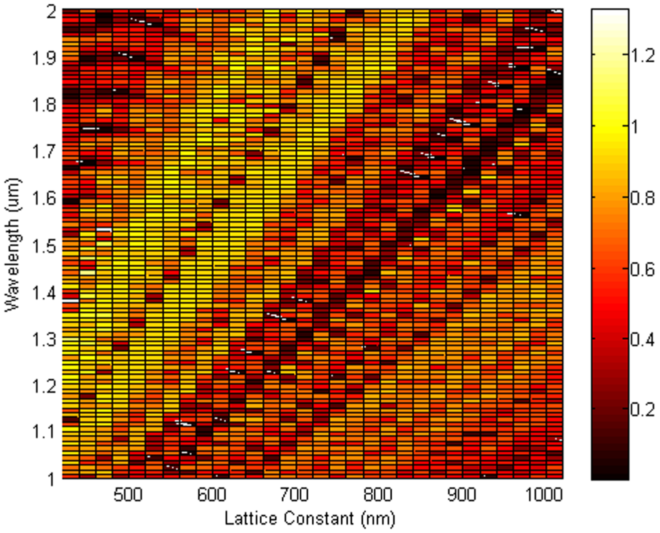

Figure 3.8: Parameter sweeps for a photonic crystal with a constant Filling Factor of 0.37 (Color showing transmission), showing the acceptance band corresponding to frequency and lattice constant variations. The normalized transmission power goes higher than 1, possibly due to cavity effects in the photonic crystal.

with minimal losses in comparison to a direct bend. The transmission in these simulations was measured with a power monitor to show the power profile of the mode in the crystal, which yielded information about transmission as seen in figure 3.9(b). By narrowing down the parameters further using the original photonic crystal simulations, a set of four released crystal parameters, and three unreleased crystal parameters were chosen to be looked at in detail in 3-D.

3.2.5 3-D FDTD Modeling

Switching to 3-D simulations leads to much larger simulation sizes and much longer simulation times. This causes a requirement of sacrificed resolution and a non-symmetric simulation mesh in all directions to alleviate the computing power necessary. Although this was the case, simulations were studied in

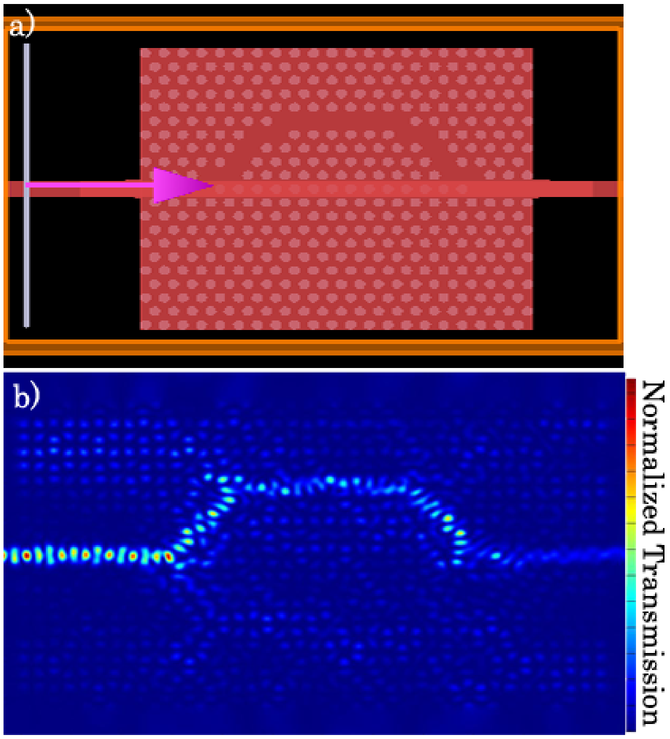

Figure 3.9: FDTD simulation of a 2-D photonic crystal with 60° bends. (a) shows the FDTD simulations layout, and (b) shows a transmission power of an injected mode at 1550 nm. As can be seen there is a lot of scattering and losses, which could be the result of a finite square mesh at hole boundaries.

detail for all narrowed down photonic crystal parameters in 3-D to attempt to get a realistic measure of light propagation in the photonic crystal device. An FDTD model of the 3-D crystal can be seen in figure 3.10, showing the eventual crystal design.

These simulations were studied in the same way as in the 2-D case, but due to the poor resolution no new information was gained. From the power monitor profiles of the 3-D devices, which were a 2-D slice taken at the center of the paddle in the out of plane direction, the parameters obtained from the 2-D simulations were confirmed in part as working for some level of transmission. Even though this was the case, the transmission seen in the profiles showed a large loss of power after the first bend, with approximately 1% or less of the power making it through. Although there were high losses showing in simula-

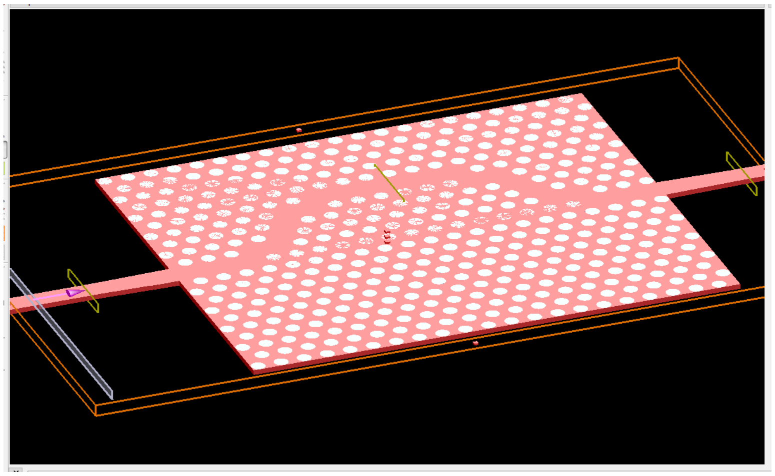

Figure 3.10: FDTD simulation model of the 3-D photonic crystal paddle suspended in vacuum.

tion, it was still assumed, based on experience gained through the photonics course that was taken as well as literature values for similar structures, that some of these parameters would lead to functional devices due to the extra losses induced by poor resolution in the circular shapes of the holes, and the massive dosage sweep done by IMEC in the fabrication process.

3.2.6 Device Design and Fabrication

Once properly simulated, a chip design was created using Design Workshop 2000 (DW2000) design software. The space on the wafer allocated for designs was $4.00 \times 0.85\,\mu$m, allowing for several device iterations. Using a grating coupler design supplied by CMC to send out of plane laser light into defined in-plane waveguides, device designs were drawn. Three basic formats of designs were chosen, including a photonic crystal paddle in a straight waveguide path, and two variations of a photonic crystal paddle embedded in a racetrack resonator. The embedded photonic crystal designs included a racetrack resonator with an add and a drop port, meaning light that coupled into the resonator would be coupled out and emitted at the drop port for detection, which results in a transmission spectrum. Also included was a racetrack resonator coupled to a single waveguide, which leads to an absorption spectrum. These two different types of spectrums come from the fact that with a single coupler, light that passes by the ring will be transferred based on the wavelength meeting the periodicity condition of the resonator, such that there will be peaks (dips) corresponding to the rings frequency response. With two coupling sections in the system, only the light that passes through the ring will be detected, which leads to a transmission spectrum giving the frequency response of the ring. The coupling distances for these waveguide to racetrack resonator devices was varied between 150-160 nm in 5 nm steps. This was done to compensate for the fact that under higher doses the line widths shrink, meaning that for ideal coupling, which was shown to be 155 nm in the simulations, the 160 nm gap would be needed.

Three basic layouts for devices were also chosen, as the exact experimental setup for measurement had not been made yet. This included designs with 4mm long grating coupler separation to allow easy free space laser coupling into devices, designs with 250 μm separations to allow fiber array coupling based on a fiber array holder in mind for the apparatus, and S-Shaped designs with ~750 μm separation to fill blank space on the chip and allow the most design iterations. This allowed for maximum leniency in apparatus design, while giving many iterations of possible working devices.

The photonic crystal design parameters used were based on FDTD simulation results previously described. To ensure full characterizations of the devices could be done, some crystals were specifically designed to work unreleased. The idea behind this was to allow characterization of the crystals properties without modulation in the signal. A list of the final design parameters can be seen in table 3.1, which shows the lattice separation constant, and the radius for each device design. It was found that the unreleased crystals had to have larger lattice separation due to the lower effective index in the material, where as the released crystals had significantly smaller lattice constants. All of the radii are given as a percentage of the lattice constant, with each being between 30-35 percent. This is seen in the literature[79, 80] as optimal radii for transmission through a triangular crystal lattice design in SOI architectures, and was backed by simulation data.

Paddle Type	Lattice Constant (nm)	Radius (% of Lattice Constant)
Unreleased	660	30
	645	31
	510	32
Released	455	34
	455	31
	450	33
	445	33

Table 3.1: Table of Device Design Parameters Used in the Final Chip Design

With all variations in devices known, a GDSII file was made for fabrication. The fabrication was done at IMEC using 193 nm deep ultraviolet lithography with a photomask. The wafer was separated into columns based on dosage rates, with dosage rates causing a 500 nm design waveguide to have an actual width ranging between 470-530 nm. The dosage curves for this process can be seen in figure 3.11 showing the variation for both waveguide lines and photonic crystal hole sizes[5]. As can be seen, the trend for line widths is to get smaller with higher dosages. This is due to the fact that light will “leak” under the solid waveguide line on the mask. For holes it has an opposite effect, since they are a lack of material the light will spread out from the edges on the mask enlarging them. With the design parameters in mind, devices were fabricated at the IMEC facility, the wafers were diced by CMC, and several dosages of chips were obtained for testing.

---

[5] Dosage curves were taken from the IMEC website at http://www2.imec.be/

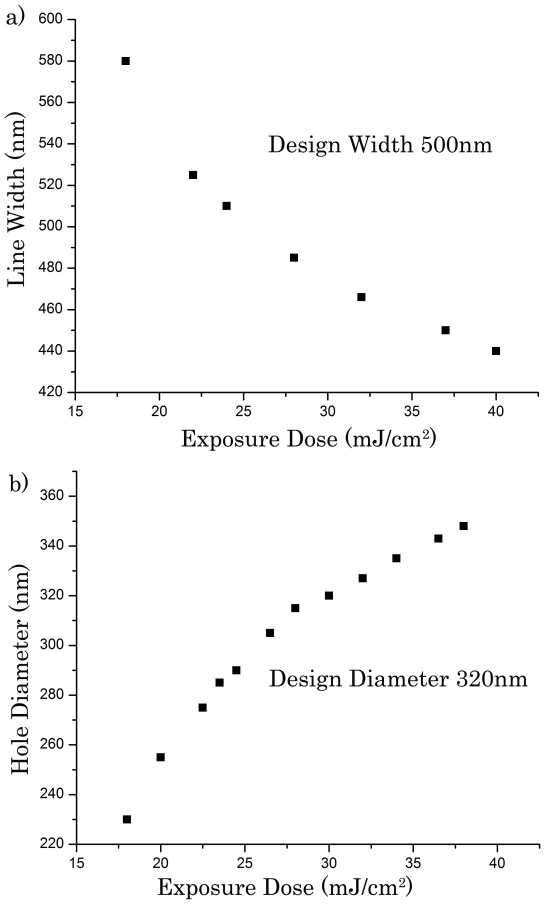

Figure 3.11: Plot showing the size scaling of (a) line elements, and (b) hole elements with respect to fabrication dosage levels at IMEC. This image has been adapted from www.imec.be.

3.2.7 Photonic Testing of Fabricated Devices

Once the chips were fabricated and returned, testing began. As added protection during shipping, a simple resist coating was layered on top. To remove this an acetone-isopropanyl-water process was done in a clean-room setting. Once the resist was removed, the chips were imaged using a SEM to obtain accurate measurements of the feature sizes. An image showing the entire design layout as well as a measurement of the hole size and separation on the +2 dosage chip can be seen in figure 3.12. This figure shows (a) a segment of the overall design layout of the devices, (b) a zoom-in of the photonic crystal paddle, and

(c) a measurement of the hole size and separation for a single devices. The parameters from this image were used to re-simulate the 3-D photonic crystal to understand the behavior of the fabricated end device.

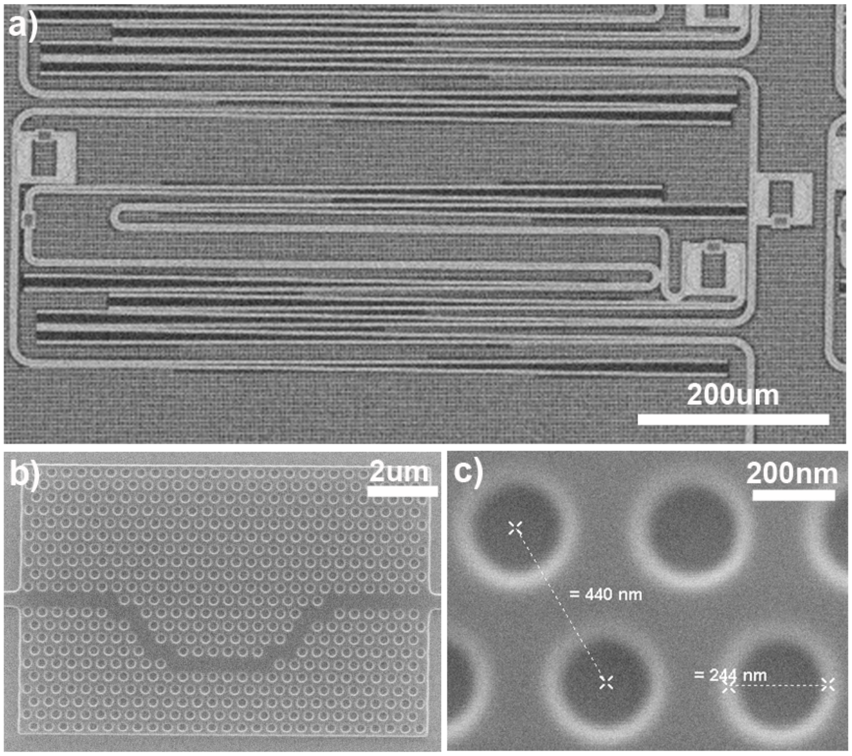

Figure 3.12: SEM image showing fabricated photonic devices. (a) shows a sample of devices included rings, gratings and photonic crystals, (b) is a zoom in of a photonic crystal showing the design of the paddle with bends, and (c) gives a measurement of the hole size and separation on a single paddle.

With the crystal measured, the photonic response of the chips was studied. This was done in the setup seen in figure 3.13, using a Santec TSL-510 tunable diode laser capable of scanning frequencies between 1500-1630 nm. By utilizing a confocal measurement setup, the impingement beam and readout beam could be translated and angled separately. This allowed for fast transitions between devices, meaning all devices could be measured in a reasonable amount of time[6].

---

[6] This excludes the previously mentioned 4mm grating separation devices designed for free space coupling.

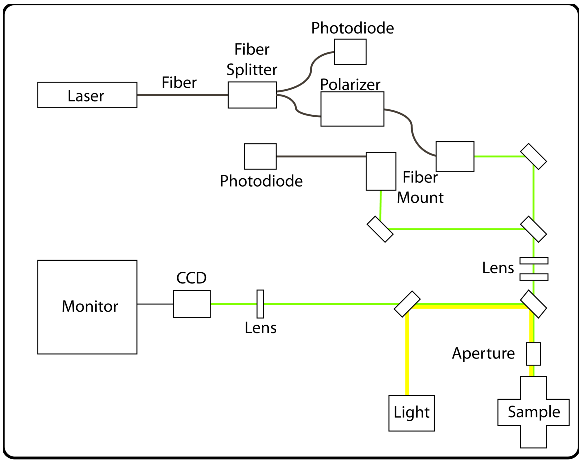

Figure 3.13: Schematic showing the measurement setup for photonic devices, using a variable diode laser and confocal setup. As can be seen, the light is fiber coupled into the confocal segment, where the focus of both the input and output beam can be separately controlled.

As can be seen in figure 3.13 the laser is directed using a fiber optic cable. This is first split with one percent of the power going to a photodiode to characterize the input power into the system, and the other ninety-nine percent passing through a fiber polarizer and into the confocal setup. The light then passes to the sample and into a device. The emitted light is then sent back to a separate fiber, which is read in through a second photodiode. To help view the system for alignment, a CCD camera with a phosphor coating was used, combined with a light for illumination.

To ensure that the response of the devices could be properly characterized, with the contributions from each individual component separated, several testing devices were incorporated on the chips overall design. The simplest of these was an input grating coupler to waveguide to output grating coupler, which was used to characterize the acceptance band of the grating couplers, as well as the losses present in the system. The response of this device can be seen in figure 3.14 which shows the output transmission of the system over a broad frequency range scanned by the laser. From this image it is clear that the grating couplers narrow the allowed frequencies in the system, as well as reducing the transmission of frequencies near the edge of the band compared to those at the center.

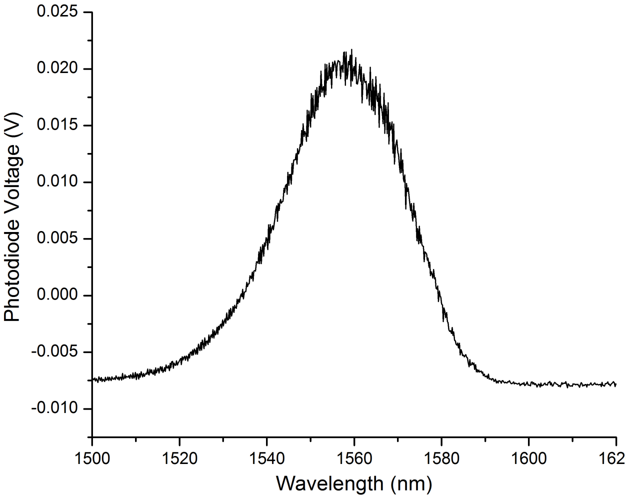

Figure 3.14: Output spectrum from a simple grating coupler to grating coupler system, over a broad laser frequency range. This figure shows the acceptance band of frequencies for the grating couplers, which defines the maximum bandwidth of any other device. The negative voltage seen is due to a DC offset in the measurement system.

Knowing the response of the grating couplers, the power spectra of both the add-drop ring resonator as well as the single waveguide coupled resonator, without a photonic crystal, was studied. The response of these systems is shown figure 3.15. Part (a) of this figure shows the absorption spectrum of a single waveguide coupled blank ring. As can be seen, the spectrum follows the same general shape as the regular transmission band of the grating couplers, except for dips corresponding to wavelengths meeting the periodic boundary conditions of light propagation in the racetrack resonator. This spectrum, establishing the free spectral range (FSR), gives information regarding the length of the racetrack resonator, the coupling efficiency between the resonator and the waveguide, and the losses present. Part (b) of figure 3.15 shows a similar spectrum for a racetrack resonator with an add/drop port. This is the inverse of the previous spectrum since the light being measured had traveled through the ring, and is also subject to higher losses due to imperfect coupling. This loss is due to the fact that, as opposed to the single coupling between the racetrack resonator and the waveguide, there are two waveguide-to-waveguide coupling segments. From these plots, the width of the FSR peaks can be measured giving ∼1-2 nm for each system, leading to Q values in the range of 1000. This response is significantly worse than optimized values in the literature [70], but is still sharp enough to be used for the purpose of a sensor.

With all of the individual components characterized, the photonic crystals were studied. Due to the fact that there were a limited number of devices optimized for non-released functionality, the results of the experiment were inconclusive as to if the devices would work. 3-D simulations of the devices were done using exact dimensions as measured by SEM images seen in figure 3.12. These simulations showed very limited transmission through the crystal, leading to the assumption that moving onto released devices would increase the odds of finding a functional photonic crystal paddle.

3.2.8 Release of Photonic Paddles

To release the paddle resonators a wet buffered oxide etch (BOE) process was needed. This required patterning of a photo-resist to selectively release a small area around the paddle. To do this a positive resist was used (ZEP520A) combined with electron beam lithography (EBL). The positive resist was chosen due to the fact that only small windows needed to be released, meaning patterning would be made easier. The process started by first cleaning the chips in

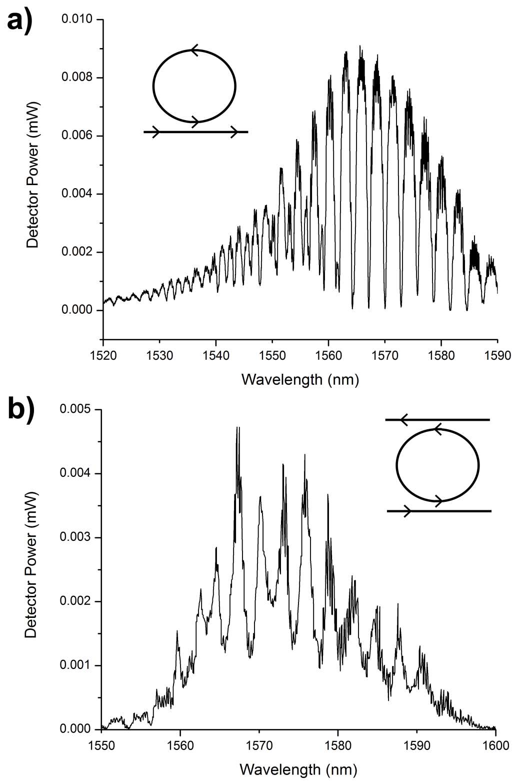

Figure 3.15: Plot showing the frequency response of (a) racetrack resonator coupled to a waveguide and (b) racetrack resonator with both add and drop ports. As can be seen, the single waveguide to ring coupling corresponds to an absorption spectrum, with the data following the initial grating coupler band. The add/drop resonator only has signal where the conditions of periodicity are met.

an acetone-IPA process to remove any particulates. With the assistance of Dr. Zhu Daio they were then layered with 200 nm coating of 1:1 ratio ZEP:anisol, which was heated and spin coated at 1500rpm. Having an approximately consistent thickness of resist on the chips[7], they were loaded into the Raith 150 EBL for patterning. From the design files, the center location of all important paddles were recorded, excluding paddles optimized for non-released functionality, and windows of approximately 18 × 12μm were exposed. Post exposure of the design, an inspection was done under an optical microscope, and the

---

[7] The thickness is approximate and not consistent across devices due to liquid tension effects near the edge of the chip cause a non-uniform thickness.

chips were stored for etching.

With the patterning done, Joe Losby assisted in the etch process of the devices. This process can be seen in 3.16, which shows the basics of how the patterning and oxide etch works. Since the BOE used is isotropic in nature (10:1 ratio of hydrofluoric acid and ammonium fluoride), the devices were etched for 20 minutes or about 1 μm of depth. This was to ensure that the paddle was completely released as well as avoiding possible stiction. With the etch done, the process was quenched using distilled water, which avoids over etching. The resist was then removed using Nano Remover PG, and the chip was submerged in isopropanol. To ensure that liquid tension did not stiction the devices during the drying process, a critical point dryer (CPD) was used. This works by replacing the isopropanol with pressurized liquid CO_2, and follows a pressure-temperature trajectory around the critical point to remove the fluid. By avoiding the liquid-vapor coexistence line, no liquid meniscus can form to draw NEMS devices towards the underlying substrate.

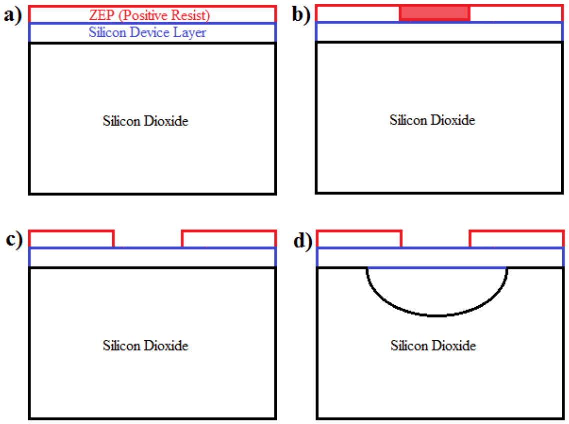

Figure 3.16: Schematic showing process for post-processing of photonic chips. (a) shows a layer of ZEP after spin coating, (b) shows the exposed ZEP for removal, (c) shows the gap left by the removal of the ZEP, and (d) shows the predicted etch of the S_iO_2 under layer.

The final released devices were inspected using SEM images and later brought into the FIB for higher resolution scans (still with SEM). An image showing a released paddle can be seen in figure 3.17, which was done using the SEM contained in the FIB chamber. From this image it is clear that the etchent caused a non-isotropic wet etch of the S_iO_2 layer, and branches out $\sim 6\mu$m from the defined window. If the BOE had behaved in a normal fashion, the maximum distance from the defined etch window would be $1\,\mu$m, which is the same as the etch depth. This resulted in a more gradual effective index change in the waveguides supporting the photonic crystal paddle, while still avoiding stiction due to the $1\,\mu$m etch depth at the actual paddle. Although the causes of this are not fully known, it is believed that due to a poor resist layer on the surface of the chip, some the the BOE was wicked ahead. This caused a brief etch of the farthest etched point, with gradually more material being removed as you approach the defined window.

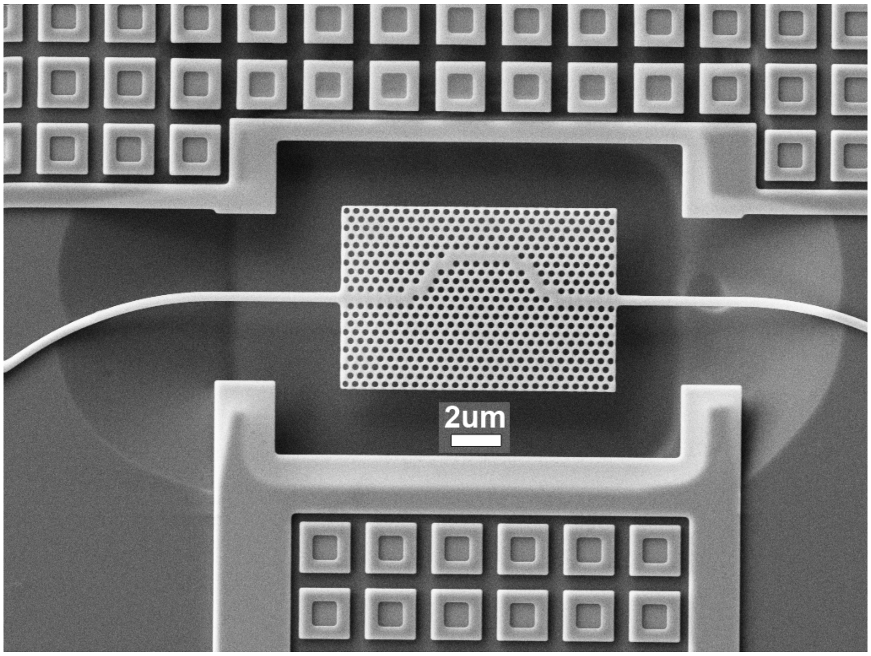

Figure 3.17: SEM image showing top down view of a released photonic crystal paddle with gently sloped etch side walls. As can be seen, the side walls extend in a slope much longer than 1μm in the direction of the torsion bars. The underlying SiO_2 layer for these devices has a thickness of 3μm, but was only etched for the 1μm mentioned above.

With the dimensions of the device known from images, a finite element simulation was done using COMSOL. This was used to determine the approximate location of each mechanical resonance frequency in the device. By building the device to the exact measured dimensions, with the exception of using square holes as opposed to circular due to processing power limitations[8], the frequencies were simulated. Although the simulations were done using accurate parameters, only the relative spacing between modes is generally accurate, as opposed to the actual frequency measurements. The simulated values of the system can be seen in table 3.2 which shows the first five eigenmodes classified as out of plane (OOP), in plane (IP), or torsional.

Mode Description	Resonance Frequency (MHz)
1st OOP	0.734
1st Torsional	1.375
1st IP	2.331
2nd OOP	2.468
2nd IP	4.699

Table 3.2: COMSOL Resonance Frequencies of Photonic Crystal Paddle, Simulated with Measured Parameters.

3.2.9 Interferometric Measurement of Paddle

Once the devices were released and free to resonate, measurement was done. The chip was mounted on a piezo buzzer using double sided tape, and then placed into a vacuum chamber with a transparent viewing window. This chamber was placed in an interferometric setup as seen in figure 3.18. A HeNe laser was focused onto the general location of the devices, and the reflection of a unfocussed beam was used to align the system. Once the laser spot was aligned to a paddle, it was re-focused and sent into the photo diode.

With a HP 8752C network analyzer both generating the drive pulse and

---

[8] Rendering circular holes requires many times more boundaries (edges) than square holes, which leads to a large increase in needed memory.

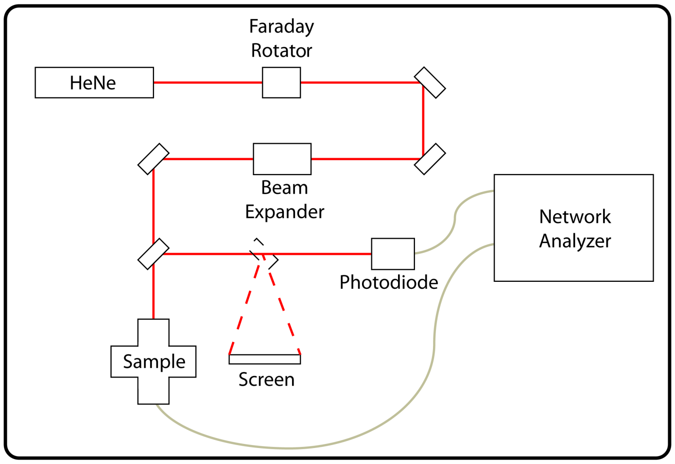

Figure 3.18: Schematic of the interferometric measurement setup for measuring released photonic crystal paddle resonators. The sample is held in a vacuum chamber, which also contains a piezo buzzer that is pulsed by the network analyzer. To view the devices for alignment, the laser can be unfocused, and a moveable mirror can be placed in the beam path to deflect it onto a screen.

measuring the response, spectrums were taken. When looking at the response of the system, it became apparent that absorption from the laser caused local heating, shifting the center frequency of resonances, as well as causing nonlinear drive at low powers. To accommodate this, the laser was left on the paddle to be measured for ∼1 hour until the temperature equilibrated, and a 20 dBm attenuator was added to the output of the network analyzer. Scans showing the first out of plane mode of a paddle can be seen in figure 3.19.

As can be seen, the first out of plane mode for the paddle resides around 600 kHz. The mode shows a large response and is close to Lorentzian shaped, as is expected, with a slight amount of non-linearity. The first out of plane mode was the only easily viewable mode from the interferometric method, which is most likely due to the fact that the piezo transducer oscillates out of plane and hence couples the best to this mode. By measuring such a response it showed that the release process did in fact work, and the devices were robust enough to handle actuation and measurement. To test that the signals were real, and correct, other contributing elements of the measurement system were ruled

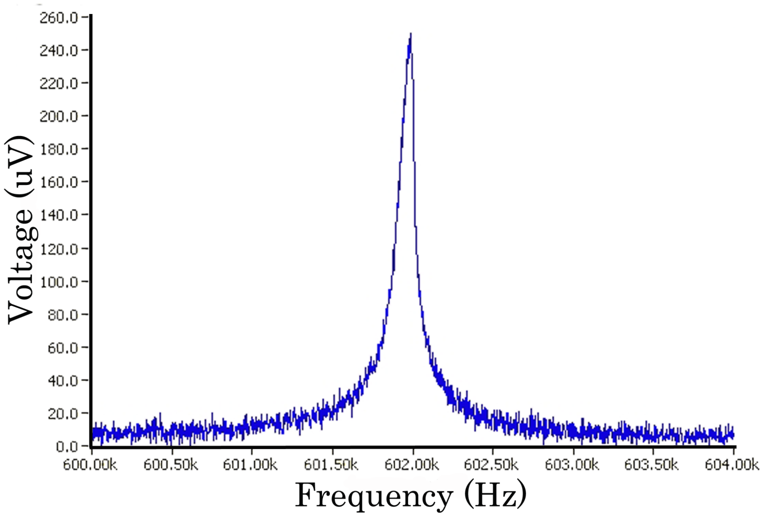

Figure 3.19: Interferometric scan of the 1st OOP mode in a paddle resonator. The frequency of the mode is in a similar position to the simulated values obtained from COMSOL.

out. The beam was blocked showing the mode disappearing, which indicates that there is no parasitic modes in the electronics. Secondly the effects with drive and the phase were looked at. These showed the mode turn nonlinear at drives higher than -10 dBm with a 20 dBm attenuator. The phase of all scans showed an inversion at the critical point on the resonances as is expected. Lastly the modes of the buzzer were checked, and can be seen in figure 3.20.

When the laser reflects off of the paddle, modulations caused by the buzzer itself is coupled in. The signal is amplified when the buzzer is on resonance, the modes of which can be seen by the dips in figure 3.20. By ruling out these modes, it was determined that the ∼600 kHz mode was in fact real, leading to a switch to photonic measurement schemes.

3.2.10 Photonic Mechanical Measurement of Paddle

With the devices working as resonators, the system was tested photonically. The principle behind the signal modulations being an effective index modulation due to changes in separation between the S_i devices layer and the S_iO_2

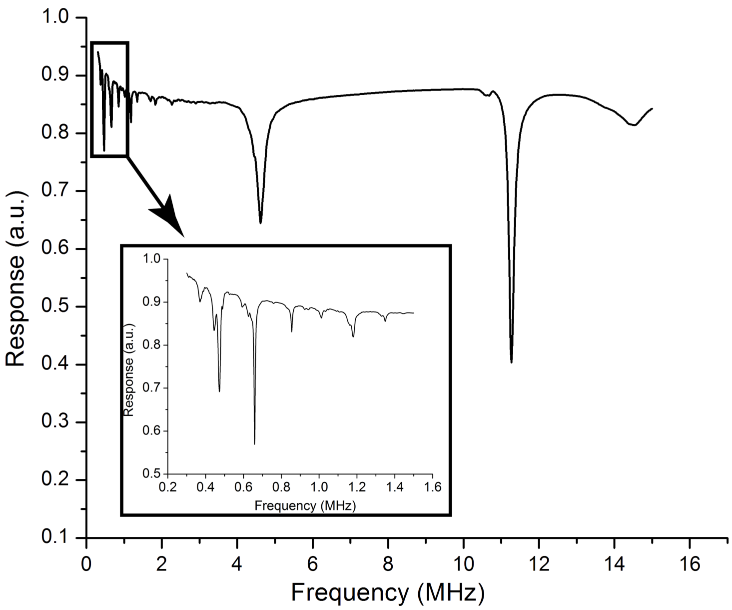

Figure 3.20: Plot showing the reflection spectrum from the piezo buzzer used. The inset shows a zoom in of the section containing the 1st out of plane resonance of the paddle.

oxide layer. To view this, the vacuum chamber was moved to the sample location in the confocal laser setup seen in figure 3.13, which has the same layout, except for the photo diode signal, which was routed to a Zurich HF2 lock-in amplifier. This lock-in amplifier provided smaller bandwidth measurements, as well superior drive control for the piezo.

To begin measurement the transmission spectra of the released devices were needed. While measuring these it became apparent that most devices on the chip did not allow for propagation of light on a detectable level. Although this was the case, devices designed for a lattice constant of 455 nm and a radius of 31% showed transmission, demonstrating that some working devices did exist. This left two 150 nm coupling devices embedded in racetrack resonators that could be measured, with the add-drop device version showing significantly broader peaks, due to coupling losses. As this was the case, all further measurements were done on a single waveguide to racetrack resonator device, whose spectrum can be seen in figure 3.21.

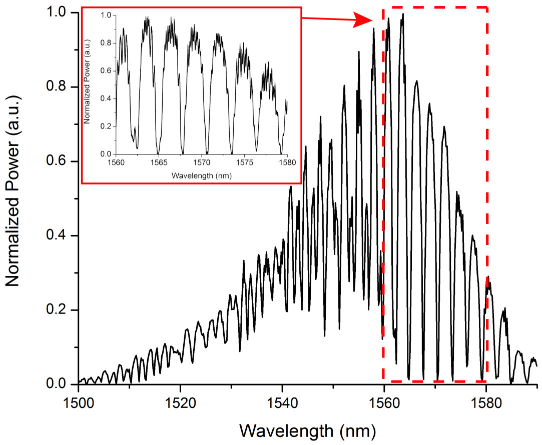

Figure 3.21: Plot showing FSR of working released paddle, with an inset showing the sharpest FSR peaks. The frequency for future measurements is kept constant at a high slope region on one of these peaks.

As can be seen, there are several well defined absorption peaks from coupling with the racetrack resonator, with high Q values ($\sim$1000). This is important as the modulation of the effective index causes an oscillation of the center frequency of the peaks, and hence with sharper peaks, more signal modulation occurs. By selecting the frequency for measurement at the steepest slope on one of these peaks, resonance modes of the device could be measured. With the operating frequency of 1561.7 μm chosen, scans of mechanical frequency space were done using the piezo buzzer. These scans showed the presence of the mode previously measured via the interferometric setup, as well as two additional modes. From the COMSOL simulation data it was determined that these modes were the first in-plane mode or second out of plane mode[9], as well as the second in-plane mode. They can be seen in figure 3.22, showing the driven signal for each mode.

Since the light in the system is propagating along the defined waveguides

---

[9] Due to a frequency overlap the exact mode shape could not be determined.

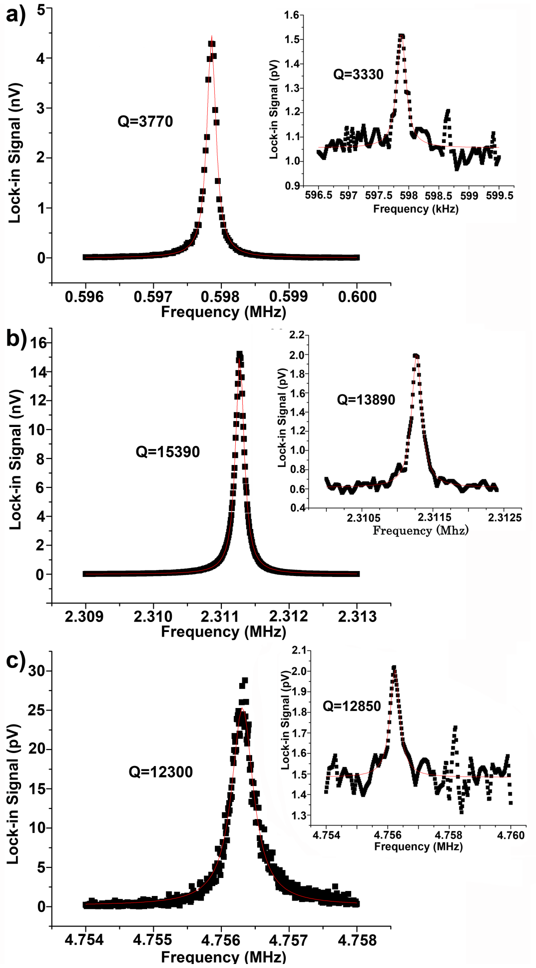

Figure 3.22: Plots showing three eigenmodes of the photonic crystal paddle with their associated thermomechanical noise peaks inset. (a) shows the 1st out of plane mode at 597.8 kHz, (b) shows the 2nd out of plane mode at 2.3112 MHz, and (c) shows the 2nd in plane mode at 4.756 MHz.

with minimal losses, there is very little heating. This allows for much cleaner and well defined peaks to be observed. With this in mind, and the fact the thermomechanical noise peaks had been observed in literature for SOI based devices[21], the modes were inspected without drive. By not only disconnecting the drive, but also capping the output to ensure no antenna effects would occur, many average scans were taken of the peaks. The time constants of these scans were made to be less than Q×T, where T stands for the period of the mode, and were averaged over hundreds of scans[10]. The results of these can be seen in the insets to figure 3.22. As can be seen from the Lorentzian fit, the Q of the thermomechanical peaks are very high and comparable to those of the driven peaks, with values reaching ∼15000. This is still low in comparison to other embedded devices in literature[21], but demonstrate the potential for the paddle as a measurement sensor.

Lastly to ensure that the devices were functioning as expected, a laser frequency sweep was done. This can be seen in figure 3.23, which shows the response of the signal at a selected drive frequency of 2.311 MHz corresponding to the second mode of the paddle. From this plot it can be seen that there are peaks roughly corresponding to the areas of highest slope, with a drop in signal around a slope of zero. This provides evidence to support the modulation of the signal coming from the phase of the device as opposed to a modulation in transmission. This fact is critical when trying to embed the photonic crystal in a high finesse cavity, as modulations based on transmission loss are less ideal.

3.3 Conclusion

A NEMS device was designed, modeled, fabricated and tested in a photonic framework. Using SOI based architecture and FDTD simulations, light propagation was studied in several photonic elements including waveguides, rings, photonic crystals, and waveguide to waveguide coupling. This gave insight into the parameters needed and the potential limitations of various device designs. With an understanding of photonics, and adequate knowledge of photonic crystals, a device design was chosen and drawn for fabrication at IMEC.

---

[10] The importance of making the scans have a time constant of less than Q×T, being that the modes energy will dissipate in that amount of time.

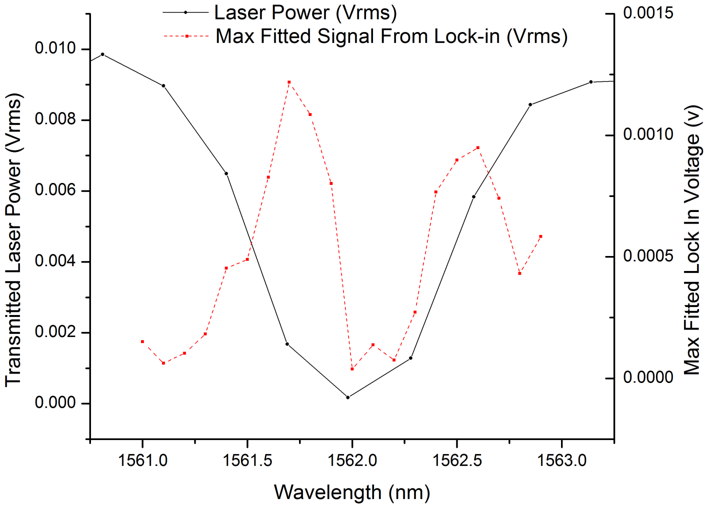

Figure 3.23: Plot showing the FSR peak of the working device with over-layed data from Lorentzian peak fits to the 2.311 MHz mechanical resonance. As can be seen the signal is the highest in regions of high slope.

A microchip containing many iterations of the device design was returned, and the photonic response of individual components what characterized using a tunable diode laser. With an adequate understanding of the devices, the photonic crystal paddles were released and studied via interferometry and photonic index modulation. The results of these studies showed the potential of photonic based measurements over interferometric, and also gave insight into improvements for future sensors.

From the results, and the fact that at least one of the fabricated devices showed potential, the experiment was deemed successful. With this working device in mind, incorporation into sensor systems can be looked at. Since the paddle design gives a platform for material to be deposited on in a regular fashion, the doors are open to almost any sensing that NEMS are capable of. Utilizing the high sensitivities seen in torsional devices, such as the device in Chapter 1, the NEMS photonic crystal paddle resonator embedded in an optical racetrack resonator has potential for improving the field of micromagnetics by allowing highly sensitive but non-invasive characterization of magnetic systems.

Chapter 4

Discussion

4.1 Summary of the Fabrication of a Single Crystalline Magnetic Garnet Disk for Torque Magnetometry

Epitaxially grown YIG was polished, milled and shaped using a FIB, into a disk of dimensions shown to support a vortex like state for the purposes of torque magnetometry. This milling process required much refining, until a segment was capable of being milled and manipulated onto a predefined and released silicon torsional resonator. This resonator was then characterized both magnetically and mechanically, with measurement and simulation, to understand the output and the potential of the device. The characterization showed a very clean magnetic response, due to lack of nanoscale magnetic disorder. During the process of milling a nano-fracture was induced in the torsional rod, which was subsequently repaired with platinum deposition. This demonstrated the robustness of the FIB giving confidence to future work.

4.2 Summary of the Design, Fabrication, and Creation of a Photonic Crystal Based Torsional Resonator

Photonics for use as a platform for NEMS was studied in full. A device design for a photonic crystal based torsional resonator was proposed, requiring simulation. Simulations of individual components, including waveguides, ring resonators and photonic crystals, were done using FDTD methods in 2 and 3-D. From these simulations the most ideal parameters were chosen for use in the design of a photonic crystal paddle resonator embedded in a high optical Q cavity. The designs were drawn, sent to IMEC for fabrication, and returned. Once cleaned of any resist, the photonic elements were characterized individually using test devices included on the chip. With an understanding of the system the devices were released and studied both interferometrically and photonically. The results of this demonstrated the power of photonic based measurement schemes, even being able to see the TM noise actuation of three eigenmodes. The overall device yielded transduction of mechanical mode, with mechanical Q values in the range of 15000.

4.3 Progress Towards a Photonics-Based Torque Magnetometer

With an understanding of torque magnetometry, and a working photonic device, the natural progression led to using the device for magnetic measurements. As a consequence of this being the first prototype of a photonic crystal paddle, no platform was left for the deposition of magnetic material. This was fixed in the second proposed version of the devices, which was not fabricated in time for this thesis. Although this meant that a simple magnetic structure could no longer be studied, a magnetic deposition could still show the potential of future devices as magnetometers. Figure 4.1 shows a proposed bar of Permalloy to be deposited onto the photonic crystal paddle.

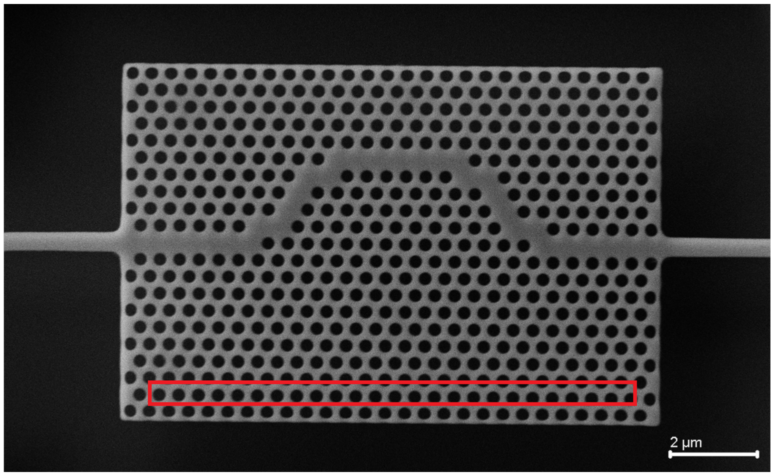

Figure 4.1: Photonic crystal paddle deposition proposal for magnetic sensing. The red box indicated the bar of Permalloy to be deposited.

Since Permalloy requires a vapor deposition, a mask was needed. This was created using a $250 \times 250\,\mu$m silicon nitride window, milled in the FIB. With the mask set, a deposition was performed by Jacob Burgess. During the process of the deposition the paddles stictioned to the underlying S_iO_2 layer, effectively ruining them for future use. The cause of this was unknown, but it was suspected that the bake-out of the sample prior to introduction into the ultra high vacuum chamber for deposition may have weakened the silicon. Future attempts to use other copies of the same devices are being planned. Ultimately the goal of an integrated photonic-based torque magnetometer will inevitably be reached.

Bibliography

[1] H. Cavendish. Experiments to Determine the Density of the Earth. *Philosophical Transactions of the Royal Society of London*, 88:469–526, 1798.

[2] H. J. Mamin and D. Rugar. Sub-attonewton force detection at millikelvin temperatures. *Applied Physics Letters*, 79(20):3358, 2001.

[3] A. N. Cleland and M L Roukes. A nanometre-scale mechanical electrometer. *Nature*, 392(March):160–162, 1998.

[4] C.A. Coulomb. *Memoires de l'Academie Royale des Sciences*. 1784.

[5] K.E. Petersen. Silicon as a mechanical material. *Proceedings of the IEEE*, 70(5):420–457, 1982.

[6] A. K. Naik, M. S. Hanay, W. K. Hiebert, X. L. Feng, and M. L. Roukes. Towards single-molecule nanomechanical mass spectrometry. *Nature Nanotechnology*, 4(7):445–450, 2009.

[7] J. W. Van Honschoten, W. W. Koelmans, S. M. Konings, L. Abelmann, and M. Elwenspoek. Nanotesla torque magnetometry using a microcantilever. In *Eurosensors XXII*, 2009.

[8] K. L. Ekinci and M. L. Roukes. Nanoelectromechanical systems. *Review of Scientific Instruments*, 76(6):061101, 2005.

[9] T. P. Burg and S. R. Manalis. Suspended microchannel resonators for biomolecular detection. *Applied Physics Letters*, 83(13):2698, 2003.

[10] Leonhard Euler. *The rational mechanics of flexible or elastic bodies 1638 - 1788*. 1960.

[11] A. N. Cleland and M. L. Roukes. Noise processes in nanomechanical resonators. *Journal of Applied Physics*, 92(5):2758, 2002.

[12] J. R. Vig and Y. Kim. Noise in microelectromechanical system resonators. *IEEE transactions on ultrasonics, ferroelectrics, and frequency control*, 46(6):1558–65, January 1999.

[13] Silvan Schmid, Sø ren Dohn, and Anja Boisen. Real-Time Particle Mass Spectrometry Based on Resonant Micro Strings. *Sensors*, 10(9):8092–8100, August 2010.

[14] N. Liu, F. Giesen, M. Belov, J. Losby, J. Moroz, A. E. Fraser, G. McKinnon, T. J. Clement, V. Sauer, W. K. Hiebert, and M. R. Freeman. Time-domain control of ultrahigh-frequency nanomechanical systems. *Nature nanotechnology*, 3(12):715–9, December 2008.

[15] C. Ke, N. Pugno, B. Peng, and H. Espinosa. Experiments and modeling of carbon nanotube-based NEMS devices. *Journal of the Mechanics and Physics of Solids*, 53(6):1314–1333, June 2005.

[16] Amir H. Safavi-Naeini, Jasper Chan, Jeff T. Hill, T. P. Mayer Alegre, Alex Krause, and Oskar Painter. Measurement of the quantum zero-point motion of a nanomechanical resonator. *Quantum*, 91125:6, 2011.

[17] Jasper Chan, T. P. Mayer Alegre, Amir H. Safavi-Naeini, Jeff T. Hill, Alex Krause, Simon Gröblacher, Markus Aspelmeyer, and Oskar Painter. Laser

cooling of a nanomechanical oscillator into its quantum ground state. *Nature*, 478(7367):89–92, October 2011.

[18] D. Karabacak, T. Kouh, and K. L. Ekinci. Analysis of optical interferometric displacement detection in nanoelectromechanical systems. *Journal of Applied Physics*, 98(12):124309, 2005.

[19] Dana Weinstein and Sunil A. Bhave. The resonant body transistor. *Nano letters*, 10(4):1234–7, April 2010.

[20] Harish Bhaskaran, Mo Li, Daniel Garcia-Sanchez, Peng Zhao, Ichiro Takeuchi, and Hong X. Tang. Active microcantilevers based on piezoresistive ferromagnetic thin films. *Applied Physics Letters*, 98(1):013502, 2011.

[21] Chi Xiong, Wolfram Pernice, Mo Li, Michael Rooks, and Hong X. Tang. Adiabatic embedment of nanomechanical resonators in photonic microring cavities. *Applied Physics Letters*, 96(26):263101, 2010.

[22] Y. T. Yang, C. Callegari, X. L. Feng, K. L. Ekinci, and M. L. Roukes. Zeptogram-scale nanomechanical mass sensing. *Nano letters*, 6(4):583–6, April 2006.

[23] V. Seena, Anukool Rajorya, Prita Pant, Soumyo Mukherji, and V. Ramgopal Rao. Polymer microcantilever biochemical sensors with integrated polymer composites for electrical detection. *Solid State Sciences*, 11(9):1606–1611, September 2009.

[24] Weibin Zhu, Jung Su Park, Jonathan L. Sessler, and Angelo Gaitas. A colorimetric receptor combined with a microcantilever sensor for explosive vapor detection. *Applied Physics Letters*, 98(12):123501, 2011.

[25] J. P. Davis, D Vick, J. A. J. Burgess, D C Fortin, P Li, V Sauer, W K Hiebert, and M R Freeman. Observation of magnetic supercooling of the transition to the vortex state. *New Journal of Physics*, 12(9):093033, September 2010.

[26] Joseph Losby, Jacob A. J. Burgess, Chris M. B. Holt, Jocelyn N. Westwood, David Mitlin, Wayne K. Hiebert, and Mark R. Freeman. Nanomechanical torque magnetometry of permalloy cantilevers. *Journal of Applied Physics*, 108(12):123910, 2010.

[27] H. J. Williams. Some Uses of the Torque Magnetometer. *Review of Scientific Instruments*, 8(2):56, 1937.

[28] J. Moreland, A. Jander, J. A. Beall, P. Kabos, and S. E. Russek. Micromechanical torque magnetometer for in situ thin-film measurements. *IEEE Transactions on Magnetics*, 37(4):2770–2772, July 2001.

[29] Thomas W Krause and D L Atherton. High resolution magnetic Barkhausen noise measurements. *NDT & E International*, 27(4):201, 1994.

[30] Alexey Kovalev, Gerrit Bauer, and Arne Brataas. Nanomechanical Magnetization Reversal. *Physical Review Letters*, 94(16):1–4, April 2005.

[31] J. Losby, J. A. J. Burgess, Zhu Diao, D. C. Fortin, W. K. Hiebert, and M. R. Freeman. In Press. *J. Appl. Phys.*, 2012.

[32] Matt Eichenfield, Christopher P. Michael, Raviv Perahia, and Oskar Painter. Actuation of micro-optomechanical systems via cavity-enhanced optical dipole forces. *Nature Photonics*, 1(7):416–422, July 2007.

[33] Bahram Jalali and Sasan Fathpour. Silicon Photonics. *Journal of Lightwave Technology*, 24(12):4600–4615, December 2006.

[34] Eugene Hecht. *Optics*. Pearson Education Inc., San Francisco, 4th edition, 2002.

[35] Henrik Sunnerud, Magnus Karlsson, and Chongjin Xie. Polarization-Mode Dispersion in High-Speed Fiber-Optic Transmission Systems. *Journal of Lightwave Technology*, 20(12):2204, 2002.

[36] E. Cortesi and F. Namavar. Novel Silicon-On-Insulator Structures for Silicon Waveguides. In *IEEE SOS/SOI Technology Conference*, volume 95, 1988.

[37] Branislav D. Timotijevic. Optical filters in silicon-on-insulator: design considerations for devices based upon strip and rib waveguides. *Proceedings of SPIE*, 6350(0):63500K–63500K–8, 2006.

[38] Graham T. Reed and Andrew P. Knights. *Silicon photonics: an introduction*. John Wiley and Sons, 2004.

[39] Fengnian Xia, Mike Rooks, Lidija Sekaric, and Yurii Vlasov. Ultra-compact high order ring resonator filters using submicron silicon photonic wires for on-chip optical interconnects. *Optics express*, 15(19):11934–41, September 2007.

[40] Sajeev John. Strong localization of photons in certain disordered dielectric superlattices. *Physical Review Letters*, 58(23):2486, 1987.

[41] Eli Yablonovitch. Inhibited Spontaneous Emission in Solid-State Physics and Electronics. *Physical Review Letters*, 58(20):2059–2062, 1987.

[42] Mo Li, W H P Pernice, C Xiong, T Baehr-Jones, M Hochberg, and H X Tang. Harnessing optical forces in integrated photonic circuits. *Nature*, 456(7221):480–4, November 2008.

[43] H. Forestier and G. Guiot-Guillain. Comptes rendus de l'Académie des sciences, 1950.

[44] R. Pauthenet. Magnetic Properties of the Rare Earth Garnets. *Journal of Applied Physics*, 30(4):S290, 1959.

[45] W. Haubenreisser. Physics of Magnetic Garnets. *Kristall und Technik*, 14(12), 1977.

[46] R. W. Cooper, W. A. Crossley, J. L. Page, and R. F. Pearson. Faraday rotation in YIG and TbIG. *Journal of Applied Physics*, 39(2):565–567, 1968.

[47] M.T. Weiss. Microwave and Low-Frequency oscillation Due to Resonance Instabilities in Ferrites. *Physical Review Letters*, 1(7), 1958.

[48] Humberto Campanella, R. P. del Real, Marina Díaz-Michelena, Marta Duch, Héctor Guerrero, Jaume Esteve, and José A. Plaza. Focused-ion-beam-assisted magnet fabrication and manipulation for magnetic field detection applications. *ACS applied materials & interfaces*, 1(3):527–31, March 2009.

[49] F. J. Rachford, M. Levy, R. M. Osgood, a. Kumar, and H. Bakhru. Magnetization and ferromagnetic resonance studies in implanted and crystal ion sliced bismuth-substituted yttrium iron garnet films. *Journal of Applied Physics*, 85(8):5217, 1999.

[50] Alastair Edward Fraser. Focused Ion Beam Milled Magnetic Cantilevers. University of Alberta, 2010.

[51] Jon Orloff, Lynwood Swanson, and Mark Utlaut William. *High resolution focused ion beams: FIB and its applications : the physics of liquid metal ion sources and ion optics and their application to focused ion beam technology.* Springer, 2003.

[52] G. Taylor. Disintegration of Water Drops in an Electric Field. *Proceedings of the Royal Society A: Mathematical, Physical and Engineering Sciences*, 280(1382):383–397, July 1964.

[53] Thoru Ishitani, Hideki Tsuboi, and Toshie Yaguchi. Transmission Electron Microscope Sample Preparation Using a Focused Ion Beam. *Journal of Electron Microscopy*, 326:322–326, 1994.

[54] K. Saitoh. Practical results of photomask repair using focused ion beam technology. *Journal of Vacuum Science & Technology B: Microelectronics and Nanometer Structures*, 6(3):1032, May 1988.

[55] A. Perentes, G. Sinicco, G. Boero, B. Dwir, and P. Hoffmann. Focused electron beam induced deposition of nickel. *Journal of Vacuum Science & Technology B: Microelectronics and Nanometer Structures*, 25(6):2228, 2007.

[56] G. Boero, I. Utke, T. Bret, N. Quack, M. Todorova, S. Mouaziz, P. Kejik, J. Brugger, R. S. Popovic, and P. Hoffmann. Submicrometer Hall devices fabricated by focused electron-beam-induced deposition. *Applied Physics Letters*, 86(4):042503, 2005.

[57] R. Lavrijsen, R. Córdoba, F. J. Schoenaker, T. H. Ellis, B. Barcones, J. T. Kohlhepp, H. J. M. Swagten, B. Koopmans, J. M. De Teresa, C. Magén,

M. R. Ibarra, P. Trompenaars, and J. J. L. Mulders. Fe:O:C grown by focused-electron-beam-induced deposition: magnetic and electric properties. *Nanotechnology*, 22(2):025302, January 2011.

[58] Dong-Hyun Kim, Elena a Rozhkova, Ilya V Ulasov, Samuel D Bader, Tijana Rajh, Maciej S Lesniak, and Valentyn Novosad. Biofunctionalized magnetic-vortex microdiscs for targeted cancer-cell destruction. *Nature materials*, 9(2):165–71, February 2010.

[59] Stuart S. P. Parkin, Masamitsu Hayashi, and Luc Thomas. Magnetic domain-wall racetrack memory. *Science (New York, N.Y.)*, 320(5873):190–4, April 2008.

[60] R. P. Cowburn, D. K. Koltsov, A. O. Adeyeye, and M. E. Welland. Single-Domain Circular Nanomagnets. *Physical Review Letters*, 83(5):1042–1045, August 1999.

[61] J. Burgess, D. Fortin, J. Losby, D. Grombacher, J. Davis, and M. Freeman. Thermally activated decay of magnetic vortices. *Physical Review B*, 82(14):1–8, October 2010.

[62] Charles Kittel. On the Theory of Ferromagnetic Resonance Absorption. *Physics Review*, 73(2):155–161, 1948.

[63] Chulmin Choi, Kunbae Noh, Young Oh, Cihan Kuru, Daehoon Hong, Diana Villwock, Li-han Chen, and Sungho Jin. Diameter-Reduced Islands for Nanofabrication Toward Bit Patterned Magnetic Media. *IEEE Transactions on Magnetics*, 47(10):2536–2539, 2011.

[64] S. H. Baek, H. W. Jang, C. M. Folkman, Y. L. Li, B. Winchester, J. X. Zhang, Q. He, Y. H. Chu, C. T. Nelson, M. S. Rzchowski, X. Q.

Pan, R. Ramesh, L. Q. Chen, and C. B. Eom. Ferroelastic switching for nanoscale non-volatile magnetoelectric devices. *Nature materials*, 9(4):309–14, April 2010.

[65] Richard A. Soref. Silicon-Based Optoelectronics. *Proceedings of the IEEE*, 81(12):1687, 1993.

[66] Anuradha M. Agarwal, Ling Liao, James S. Foresi, Marcie R. Black, Xiaoman Duan, and L. C. Kimerling. Low-loss polycrystalline silicon waveguides for silicon photonics. *Journal of Applied Physics*, 80(11):6120, 1996.

[67] M. Elkurdi, S. David, X. Checoury, G. Fishman, P. Boucaud, O. Kermarrec, D. Bensahel, and B. Ghyselen. Two-dimensional photonic crystals with pure germanium-on-insulator. *Optics Communications*, 281(4):846–850, February 2008.

[68] P Nellen, P Strasser, V Callegari, R Wuest, D Erni, and F Robin. Focused ion beam modifications of indium phosphide photonic crystals. *Microelectronic Engineering*, 84(5-8):1244–1247, May 2007.

[69] E. Yablonovitch and TJ Gmitter. Photonic band structure: The face-centered-cubic case. *Physical Review Letters*, 63(18):1950, 1989.

[70] Jan Niehusmann, Andreas Vörckel, Peter Haring Bolivar, Thorsten Wahlbrink, and Wolfgang Henschel. Ultrahigh-quality-factor silicon-on-insulator microring resonator. *Optics Letters*, 29(24):2861, 2004.

[71] E. A. J. Marcatili. Bends in optical dielectric guides. *Bell System Technical Journal*, 48:2103, 1969.

[72] Kane S. Yee. Numerical Solution of Initial Boundary Value Problems Involving Maxwell's Equations in Isotropic Media. *IEEE Transactions on Antennas and Propagation*, 14(3):303, May 1966.

[73] A. Taflove. Application of the finite-difference time-domain method to sinusoidal steady-state electromagnetic-penetration problems. *Electromagnetic Compatibility, IEEE Transactions*, 22(3):191, 1980.

[74] A. Lavrinenko, P. Borel, L. Frandsen, M. Thorhauge, A. Harpoth, M. Kristensen, T. Niemi, and H. Chong. Comprehensive FDTD modelling of photonic crystal waveguide components. *Optics express*, 12(2):234–48, January 2004.

[75] Amir Hosseini, Hamid Nejati, and Yehia Massoud. Modeling and design methodology for metal-insulator-metal plasmonic Bragg reflectors. *Optics express*, 16(3):1475–80, February 2008.

[76] D. M. Sullivan. A frequency-dependent FDTD method for biological applications. *IEEE Transactions on Microwave Theory and Techniques*, 40(3):532–539, March 1992.

[77] W. H. P. Pernice, Mo Li, and Hong X. Tang. Optomechanical coupling in photonic crystal supported nanomechanical waveguides. *Optics express*, 17(15):12424–32, July 2009.

[78] A. Mekis, J. C. Chen, I. Kurland, S. Fan, P. R. Villeneuve, and J. D. Joannopoulos. High Transmission through Sharp Bends in Photonic Crystal Waveguides. *Physical review letters*, 77(18):3787–3790, October 1996.

[79] L Frandsen, A. Harpoth, P. Borel, M. Kristensen, J. Jensen, and O. Sigmund. Broadband photonic crystal waveguide 60 degrees bend obtained

utilizing topology optimization. *Optics express*, 12(24):5916–21, November 2004.

[80] A. Birner, R. B. Wehrspohn, U. M. Gösele, and K. Busch. Silicon-Based Photonic Crystals. *Advanced Materials*, 13(6):377–388, March 2001.

[81] W. H. P. Pernice, M. Li, D. F. G. Gallagher, and H. X. Tang. Silicon nitride membrane photonics. *Journal of Optics A: Pure and Applied Optics*, 11:114017, 2009.